# Hierarchical superparamagnetic Metal-Organic Frameworks nanovectors as anti-inflammatory nanomedicine.†

Heng Zhao,[a] Saad Sene,[b] Angelika M. Mielcarek,[a] Sylvain Miraux,[c] Nicolas Menguy,[d] Dris Ihiawakrim,[e] Ovidiu Ersen,[e] Christine Péchoux,[f] Nathalie Guillou,[b] Joseph Scola,[g] Jean-Marc Grenèche,[h] Farid Nouar,[a] Simona Mura,[i] Florent Carn,[j] Florence Gazeau,[j] Eddy Dumas,[b] Christian Serre,*[,a] and Nathalie Steunou*[,a,b]

[a]Institut des Matériaux Poreux de Paris, ENS, ESPCI Paris, CNRS, PSL university, Paris, France. E-mail: christian.serre@ens.fr, nathalie.steunou@uvsq.fr

[b]Institut Lavoisier de Versailles, UMR CNRS 8180, Université de Versailles St Quentin en Yvelines, Université Paris Saclay, Versailles, France.

[c]Centre de Résonance Magnétique des Systèmes Biologiques, UMR5536, CNRS/Univ. Bordeaux 33076 Bordeaux, France.

[d]Sorbonne Université, UMR CNRS 7590, MNHN, IRD, Institut de Minéralogie, de Physique des Matériaux et de Cosmochimie, IMPMC, 75005 Paris, France.

[e]Institut de Physique et Chimie des Matériaux de Strasbourg (IPCMS) UMR 7504 CNRS – Université de Strasbourg, 23 rue du Loess 67034 Strasbourg Cedex 2, France.

[f]Université Paris-Saclay, INRAE, AgroParisTech, GABI, 78350, Jouy-en-Josas, France.

[g]Groupe d'Etudes de la Matière Condensée, UMR CNRS 8635, Université de Versailles St Quentin en Yvelines, Université Paris Saclay 78035 Versailles, France.

[h]Institut des Molécules et des Matériaux du Mans, UMR CNRS 6283, Université du Maine, 72085 Le Mans, France.

[i]Institut Galien Paris-Saclay, UMR 8612, CNRS, Université Paris-Saclay, Faculté de Pharmacie, 5 rue Jean-Baptiste Clément, F92296 Châtenay-Malabry cedex, France.

[j]Laboratoire Matière et Systèmes Complexes (MSC), UMR CNRS 7057, Université de Paris, 75013 Paris, France.

†Electronic Supplementary Information (ESI) available: [details of any supplementary information available should be included here]. See DOI: 10.1039/x0xx00000x

Among a plethora of drug nanocarriers, biocompatible nanoscale Metal Organic Frameworks (nanoMOFs) with large surface area and amphiphilic internal microenvironment have emerged as promising drug delivery platforms, mainly for cancer therapy. However, their application in biomedicine still suffers from shortcomings such as a limited chemical and/or colloidal stability and/or toxicity. Here, we report the design of a hierarchically porous nano-object (denoted as USPIO@MIL) combining a benchmark nanoMOF, (*that is,* the MIL-100(Fe)), and ultra-small superparamagnetic iron oxide (USPIO) nanoparticles, (*that is,* maghemite), that is synthesized through a one-pot, cost-effective and environmentally friendly protocol. The synergistic coupling of the physico-chemical and functional properties of both nanoparticles confer to these nano-objects valuable features such as high colloidal stability, biodegradability, low toxicity, high drug loading capacity as well as stimuli-responsive drug release and superparamagnetic properties. This bimodal MIL-100(Fe)/maghemite nanocarrier once loaded with anti-tumoral and anti-inflammatory drugs (doxorubicin or methotrexate), leads to high anti-inflammatory and anti-tumoral activities. In addition, USPIO@MIL nano-object presents excellent relaxometric properties and its applicability as an efficient contrast agent for magnetic resonance imaging is herein demonstrated. This highlights the high potential of maghemite@MOF composite integrating the functions of imaging and therapy as theranostic anti-inflammatory formulation.

## Introduction

Inflammation is a complex mechanism of the body's defense, arising from multiple causes such as infectious agents (viruses, bacteria), radical oxygen species or metabolic stress (hypoxia). A large spectrum of pathologies such as sepsis, asthma, type 2 diabetes, neurodegenerative, cardiovascular and intestinal diseases, rheumatoid polyarthritis and also cancer are accompanied by an uncontrolled inflammatory response. The conventional treatment of such inflammatory diseases generally relies on the use of steroidal or nonsteroidal anti-inflammatory drugs, as well as anti-leukotrienes or pro-inflammatory cytokine inhibitors.[1] However, these treatments often lack from an optimal

pharmacological activity as a result of non-specific biodistribution, low bioavailability and/or short half-life into the body, together with high dosages required associated to off-target side effects.[1] To overcome such drawbacks, nanomedicines based on nanoparticles (NPs) such as liposomes loaded with anti-inflammatory drugs were developed and have shown therapeutic improvements of inflammatory diseases in pre-clinicals studies.[1] They were also applied in cancer treatment due to the relation observed between the tumor inflammatory microenvironment and cancer carcinogenesis, dissemination and metastasis.[2] However, only a very limited number of anti-inflammatory nanomedicines have succeeded to reach clinical trials.[3] Among key issues to be addressed, one can point out their insufficient stability in biological fluids, low drug loading capacity, uncontrolled drug delivery as well as their limited biocompatibility and safety.[1, 3] More importantly, their complex architecture often requires a multi-step synthesis which is a strong hurdle for the cost-effective scaling-up of their production. There is thus an urgent need to develop a novel generation of anti-inflammatory nanomedicines.

In this context, Metal Organic Frameworks (MOFs) have recently emerged as alternative drug-delivery platforms. MOFs are micro- or meso-porous crystalline hybrid materials consisting of metal ions, clusters or chains interconnected by organic linkers.[4-8] Their unprecedented chemical and structural diversity,[4-8] high surface area as well as their suitable amphiphilic internal microenvironment, make these solids promising drug nanocarriers. Not only are these latter able to encapsulate a high diversity of active ingredients (drugs, biological gases, proteins, photosensitizers…) but their drug loading capacities can reach record values, up to 2 g of drug per gram of empty MOF, surpassing those of any other drug nanocarrier.[9] Moreover, through a careful choice of the MOF and depending on the administration route, one can achieve in most cases a controlled, progressive, eventually stimuli-responsive, drug release, avoiding a therapeutically inactive burst-release. The combination of a wide range of metal clusters and organic linkers contributes to their compositional and structural tunability and endows them multiple functionalities of interest for therapy, diagnosis and imaging, thereby allowing the construction of theranostics nanovector.[10-16] The therapeutic efficiency of these

nanoMOFs can be further enhanced by integrating another material such as metals, metal oxide NPs, (bio)polymers, enzymes, or nucleic acids, either anchored at the surface of nanoMOFs or alternatively encapsulated within their internal porosity.[17-20] While polymer coating has been shown to enhance the pharmacokinetics of MOF NPs (colloidal stability and blood circulation time), metal and metal oxide NPs could confer magnetic, plasmonic or luminescent properties of interest for multimodal imaging and diverse therapies (photothermal and photodynamic).[10-19, 21-22] Although significant progress has been achieved in this field, such nanoMOFs still face critical issues that are detrimental for their biomedical application. Due to their complex microstructure and multi-component composition, most MOFs nanocarriers present a high toxicity and/or a poor chemical or colloidal stability while their biodegradability or intracellular fate was rarely evaluated.[23] So far MOF platforms were reported mainly for cancer therapy[9-16] while their potential has barely been explored for inflammatory chronic diseases such as rheumatoid arthritis (RA).[24-29] Moreover, these nanovectors are often prepared through complicated, multi-steps and time-consuming synthesis procedures relying on the use of organic solvents hampering their clinical translation.

In light of these developments, some of us have reported in the past few years nano-objects (denoted as MIL/USPIO-cit) that consisted of mesoporous $Fe^{3+}$ trimesate MOF (*i.e.* MIL-100(Fe)) NPs whose outer surface was post-synthetically coated by citrate modified maghemite $\gamma$-$Fe_2O_3$-cit NPs.[18] Such USPIO NPs were selected due to their superparamagnetic properties and their efficiency as $T_2$ MRI contrast agent. Although this MIL/USPIO-cit nanovector was shown to be a promising candidate for cancer theranostics, its $\gamma$-$Fe_2O_3$-citrate did not exceed 10 wt% and its colloidal stability was not optimal in physiological conditions.[18]

In the present article, we have developed a novel hierarchical superparamagnetic and stimuli-responsive nano-object (denoted as USPIO@MIL) (Scheme 1) that consists of small MIL-100(Fe) NPs (50 nm) in which $\gamma$-$Fe_2O_3$ NPs are homogeneously distributed in their core and at their surface. Our objective was to design one single multifunctional nanostructure integrating the therapeutic functions of the MOF (drug delivery properties) with the diagnostic ability of $\gamma$-$Fe_2O_3$ ($T_2$ contrast agent in MRI).

This bimodal nanovector was synthesized through a direct cost-effective room temperature (RT) green approach. Two complementary anti-cancer and anti-inflammatory drugs (either doxorubicin (Dox) or methotrexate (MTX)) were encapsulated with a high drug loading in this bimodal nanovector to synergistically target both malignant cells and tumor inflammatory components. Indeed, Dox, a widely used anticancer drug has also shown its capacity to induce apoptosis of inflammatory neutrophils[30-31] while MTX is not only a chemotherapy agent but also the first-line conventional drug for rheumatoid arthritis (RA). Our objective was thus to design a novel type of nanomedicine for the treatment of chronic inflammatory disease such as RA. Note that RA is frequently accompanied by other diseases such as cancer[32] that can affect all body organs with however, to date, no effective available therapy targeting simultaneous cancer and RA.[30-32] This USPIO@MIL nanovector and drug loaded analogues present a low cytotoxicity while their biodegradability was demonstrated through their internalization in macrophages and intracellular fate monitored by TEM. Remarkably, the stimuli-responsive drug release properties of USPIO@MIL/Dox (and also USPIO@MIL/MTX to a less extent) confer to these nanovectors a high anti-tumoral and anti-inflammatory capability. Finally, USPIO@MIL nano-object exhibits a superparamagnetic behaviour suitable for its use as *in vivo* contrast agent for MRI, thereby paving the way for its applicability in image-guided therapy to diagnose and treat inflammatory diseases.

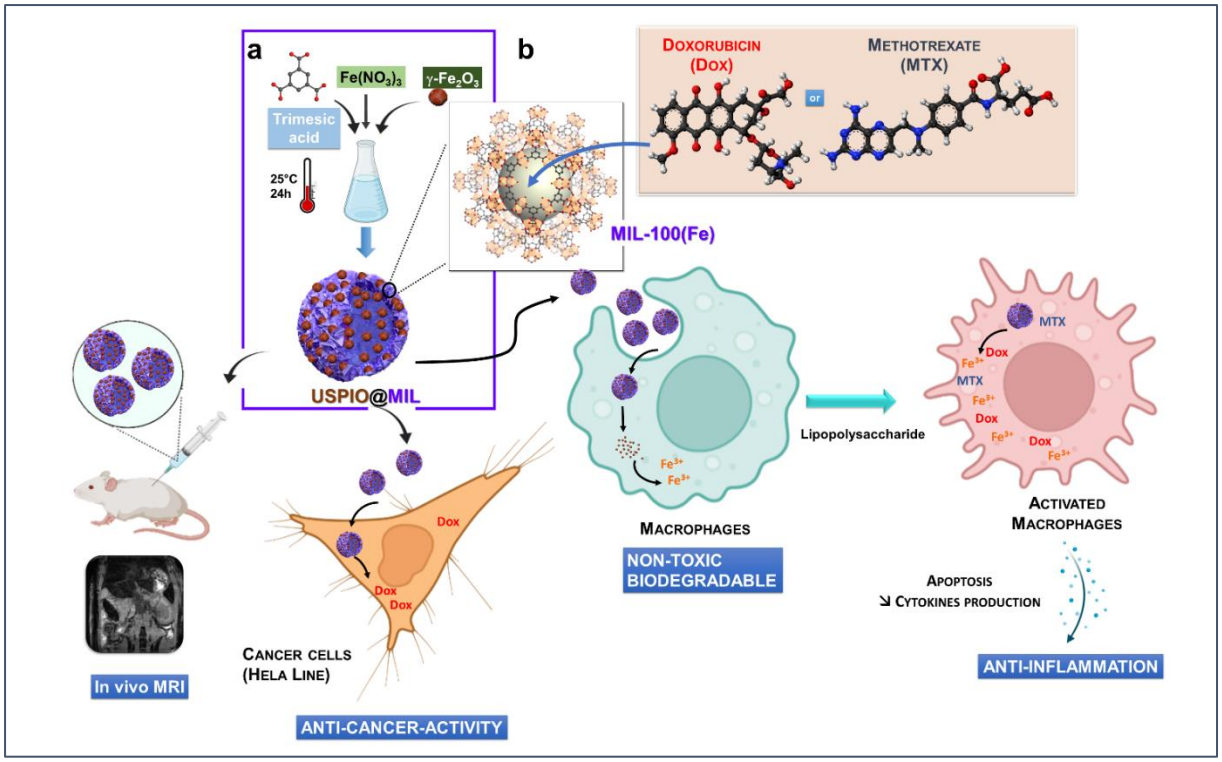


**Scheme 1** Schematic illustration of a) synthesis of USPIO@MIL-100(Fe) nano-objects and b) their use as a theranostic platform for the treatment of cancer and inflammatory diseases.

## Results and Discussion

### Synthesis of maghemite embedded MIL-100(Fe) nano-objects

The synthesis of USPIO@MIL nano-objects was derived from a protocol recently developed by some of us for the preparation of MIL-100(Fe) NPs (Fig. S1 and S2, ESI).[33] This procedure consists of mixing the iron salt and the benzene tricarboxylic acid (1,3,5-BTC) ligand in water at RT, which is advantageous compared to conventional solvothermal synthesis (reflux or microwave), both from a technico-economic point of view and for the preparation of MOF-composites relying on fragile nano-objects (NPs, enzymes…).[33-35] Firstly, the USPIO NPs were prepared by a coprecipitation method according to well-known procedures.[36-37] Their characterization by using PXRD, HRTEM, FT-IR, DLS and $^{57}$Fe Mössbauer spectrometry have clearly shown the formation of maghemite (*i.e.* $\gamma$-$Fe_2O_3$) NPs with a cubic deficient spinel structure (a = 0.836 (1) nm) and a particle diameter close to 7 nm (Fig. S3, ESI). Then, the USPIO@MIL nano-objects were then synthesized following an *in situ* approach, where the

nanoMOF was formed at RT in the presence of $\gamma$-$Fe_2O_3$ NPs as a co-reactant in a reaction medium containing the iron salt and the organic ligand, keeping the same reaction conditions as those used for the bare MIL-100(Fe) (see ESI for details).[33] First, the USPIO@MIL nano-objects were prepared with a content of $\gamma$-$Fe_2O_3$ of 20 wt% (referred as USPIO(20)@MIL) as shown by the combination of Inductively Coupled Plasma Mass Spectroscopy (ICP-MS) and High Performance Liquid Chromatography (HPLC) (Table S1, Fig. S4, ESI). The nano-objects have been fully characterized by combining PXRD, DLS, TEM, HAADF-STEM, $N_2$ porosimetry and FTIR (Fig. 1, 2 and S5-S7, ESI). PXRD pattern of USPIO(20)@MIL superimposes well with those of both MIL-100(Fe) and $\gamma$-$Fe_2O_3$, according to the structureless refinement performed for maghemite and the profile matching for the MOF (Fig. 1a). Accordingly, the TEM and HAADF-STEM (Fig. 1 and S7, ESI) images show that USPIO(20)@MIL consists of spheroidal particles of 56 ± 11 nm in diameter with a small size distribution which is close to the dimensions of the bare nanoMOF (40 ± 8 nm) (Fig. S2, ESI). Note that the diameter and particle size distribution of MIL-100(Fe) NPs in USPIO(20)@MIL are significantly lower than that of MIL-100(Fe) NPs prepared by microwave assisted solvothermal protocol.[18, 38-39] The TEM and HAADF-STEM images show that the outer surface of USPIO@MIL NP is partially decorated by small aggregates of $\gamma$-$Fe_2O_3$ NPs while a minor amount of individual $\gamma$-$Fe_2O_3$ NPs is observed (Fig. 1) on the TEM images. Electron tomography experiments were performed to further analyze the 3D architecture of USPIO(20)@MIL nanostructures and elucidate the location of the $\gamma$-$Fe_2O_3$ NPs. Degradation of the nanoMOF is observed upon exposure to the electron beam but it does not affect the observation of the embedded $\gamma$-$Fe_2O_3$ NPs. According to the 3D reconstruction of the USPIO(20)@MIL nano-objects, the $\gamma$-$Fe_2O_3$ NPs are concomitantly located at the outer surface of the MIL-100(Fe) NPs and also embedded in their core (Fig. 2). This suggests that these entrapped $\gamma$-$Fe_2O_3$ NPs may act as anchors for the initial formation of MIL-100(Fe) seeds, followed by their further outward growth, gradually forming the hierarchical porous USPIO(20)@MIL NPs, with the remaining USPIO being attached at the external surface of the composite. The spatial distribution and organization of $\gamma$-$Fe_2O_3$ NPs is different whether they are located at the surface or in the core of MIL-100(Fe). While a large number of $\gamma$-$Fe_2O_3$ NPs are

strongly aggregated at the surface of nanoMOFs, they are randomly spatially distributed in the core of MIL-100(Fe). According to electron tomography, one can estimate a similar relative amount of the "surface" and "embedded" $\gamma$-$Fe_2O_3$ NPs within USPIO(20)@MIL although this quantification could only been performed on a limited number of nano-objects. The stoichiometry of iron oxides in USPIO(20)@MIL was finally assessed by $^{57}$Fe Mössbauer spectrometry (300 and 77 K) in order to exclude a possible reduction of $\gamma$-$Fe_2O_3$ to $Fe_3O_4$ magnetite NPs during the formation of USPIO(20)@MIL. Note that both iron oxides cannot easily be distinguished by PXRD since they exhibit the inverse spinel crystalline structure with a close lattice parameter. The $^{57}$Fe Mössbauer spectrum of USPIO(20)@MIL recorded at 77 K (see ESI for details and Fig. S14) shows a broadened lines sextet that can be assigned to $\gamma$-$Fe_2O_3$ NPs while the central asymmetrical quadrupolar doublet results from both MIL-100(Fe) and small non-interacting $\gamma$-$Fe_2O_3$ NPs. The acquisition of $^{57}$Fe Mössbauer spectra at both 300 K and 77 K allows thus to identify the presence of interacting and non-interacting $\gamma$-$Fe_2O_3$ NPs located presumably at the surface and in the core of MIL-100(Fe) particles as shown by TEM and electron tomography. The relative amount of both MIL-100(Fe) and $\gamma$-$Fe_2O_3$ estimated from the respective absorption areas (69% and 31%) is fully consistent with the quantification given by ICP-MS and HPLC (see above).

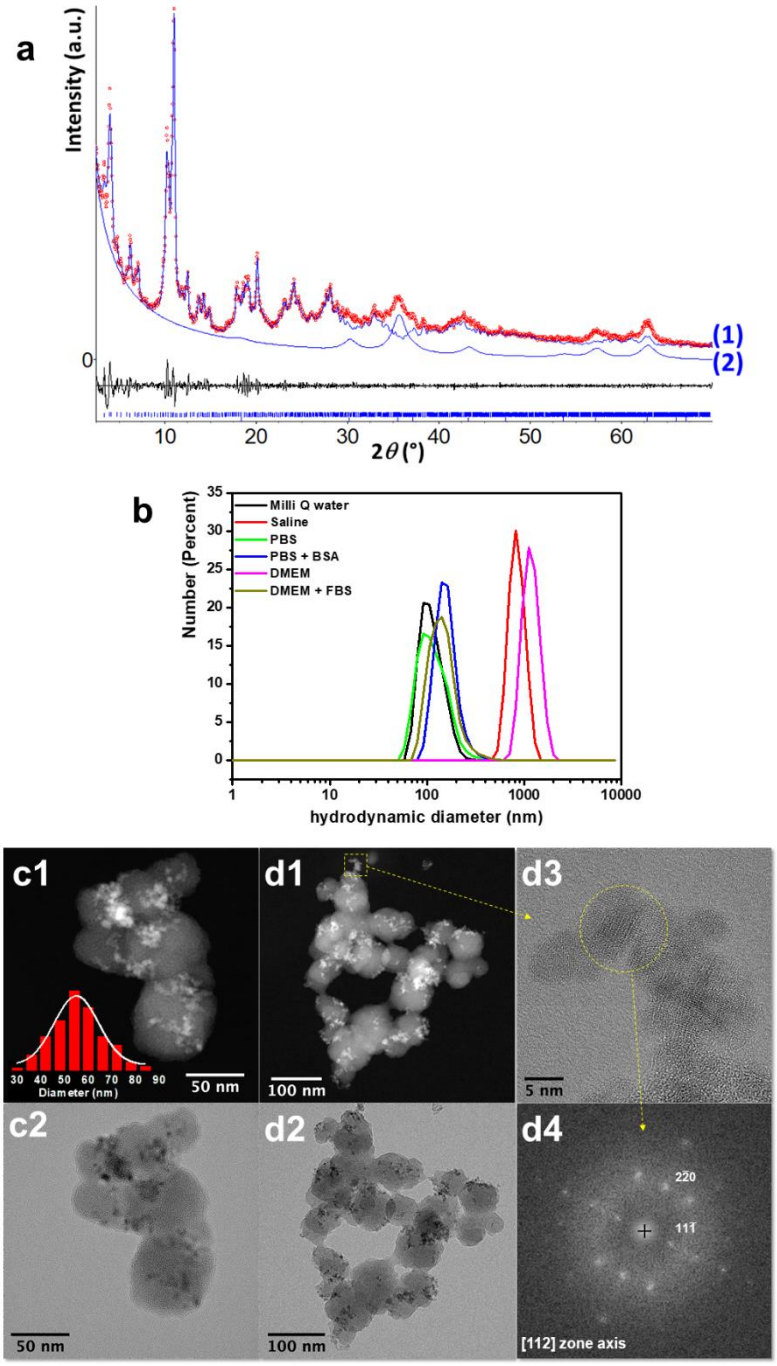


**Fig. 1** Characterizations of USPIO(20)@MIL. a) Refinement of USPIO(20)@MIL PXRD pattern (Rietveld refinement was performed for maghemite whereas a profile pattern matching was undertaken for the MIL-100(Fe) contribution) (λCu ≈ 1.5418 Å) The red points correspond to the observed data and the black linee to the difference curve. Calculated contributions of the MIL-100(Fe) (1) and $\gamma$-$Fe_2O_3$ (2) are represented in blue; b) Hydrodynamic diameters of USPIO(20)@MIL at a concentration of 200 $\mu g.mL^{-1}$ in different media (Milli Q water, Saline, PBS, PBS + BSA, DMEM and DMEM + FBS) at RT. (c1-d1) STEM-HAADF and corresponding (c2-d2) TEM-BF images of USPIO(20)@MIL. (d3) HRTEM image of USPIO with (d4) FFT indexed with the cubic cell ($a$ = 0.8346 nm). Inset of c1) particle size distribution (diameter = 56 ± 11 nm) of USPIO(20)@MIL NPs.

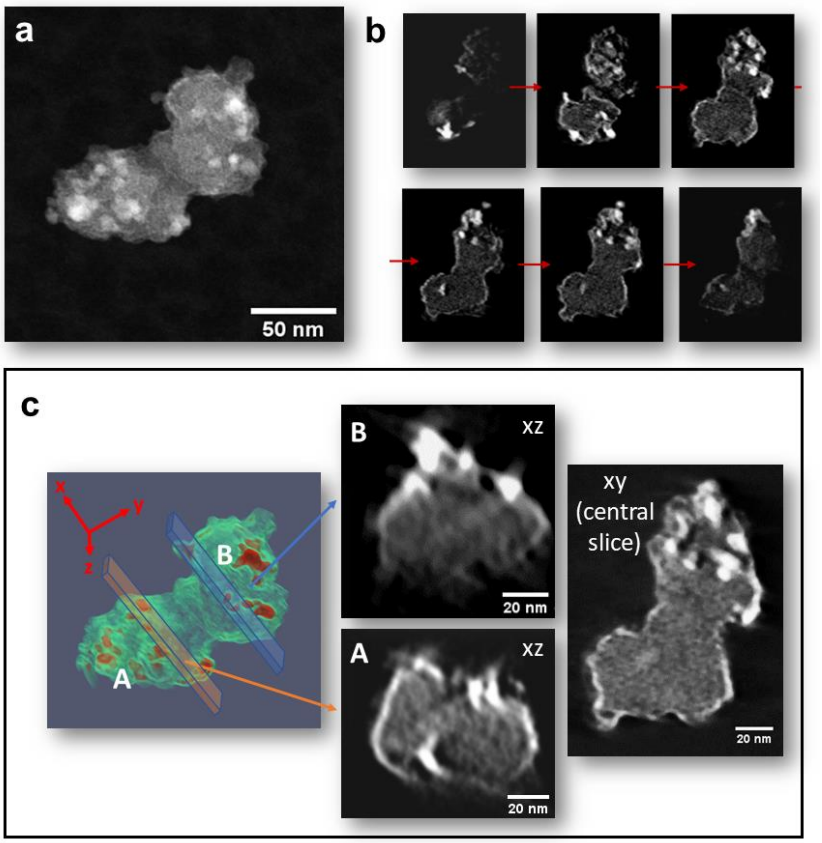


**Fig. 2** Electron tomography analysis of two typical aggregated USPIO(20)@MIL nano-objects. a, b) STEM-HAADF images, at 0° tilt, from the tilt series used to reconstruct the volume (a) and several slices extracted from the bottom to the top of the volume of the aggregate obtained by reconstruction (b); c) The 3D model of the two aggregated USPIO(20)@MIL nano-objects with $\gamma$-$Fe_2O_3$ NPs in red and MIL-100(Fe) NPs in green and three corresponding slices through the reconstruction parallel to either (xz) or (xy) planes.

Similar USPIO(10)@MIL nanostructures with a lower $\gamma$-$Fe_2O_3$ content of 10 wt% could also be synthesized at RT by the *in situ* approach as shown by PXRD, $N_2$ porosimetry, TGA and TEM (Fig. S8). This shows that the *in situ* route allows to tune the rate of USPIO while preserving the microstructure of nano-objects. For both USPIO(X)@MIL (X=10 and 20), the TEM images show clearly that a negligible amount of USPIO was physically separated from MIL-100(Fe) NPs (Fig. 1, S7 and S8, ESI), thus located either at the surface or embedded in the core of the nanoMOF. This is in contrast to the previously reported MIL/USPIO-cit nano-objects whose maximum thresholds could not exceed 10 wt% above which $\gamma$-$Fe_2O_3$ aggregates are simultaneously formed.[18] This clearly shows that the *in situ* approach can produce homogeneous USPIO@MIL nano-objects with a maghemite rate as high as 20 wt%.

**Colloidal stability in serum conditions**

To assess their intravenous administration and potential use as drug delivery systems, the colloidal stability of USPIO(20)@MIL was studied under different simulated physiological medium conditions. In contrast to a strong aggregation observed in the Dulbecco's Modified Eagle Medium (DMEM) cell culture medium, saline solution (0.9% NaCl) and phosphate buffer saline (PBS), an excellent colloidal stability of USPIO(20)@MIL NPs was observed in Milli Q water, in DMEM supplemented with fetal bovine serum (FBS) (10% v/v) and in PBS supplemented with bovine serum albumin (BSA) (5.4% v/v) since their hydrodynamic diameter (*i.e.* ~140, 150 and 170 nm, respectively) remained constant for 24 h (Fig. 1b and S9, ESI). Interestingly, as previously reported for MIL/USPIO-cit,[18] the long term colloidal stability of USPIO(20)@MIL NPs was significantly enhanced by using DMEM and PBS buffer solutions containing serum and thus the most abundant plasma proteins in mammals, albumin (Fig. S10 and S11, ESI). This may result from a possible adsorption of BSA at the surface of NPs as reported before.[18, 40] It is worth noting that USPIO(20)@MIL NPs exhibit a superior colloidal stability in comparison to that of MIL/USPIO-cit NPs[18] as a result of their smaller mean diameter (170 nm for USPIO(20)@MIL and 380 nm for MIL/USPIO-cit) in PBS/BSA, which is beneficial for their intravenous administration. The long-term chemical stability of MIL-100(Fe) and USPIO(20)@MIL in PBS and PBS/BSA solutions was finally investigated by varying pH. According to the PXRD and TEM experiments (Fig. S12 and S13, ESI), USPIO(20)@MIL NPs exhibit a good stability in PBS and PBS/BSA solutions at pH 5.1 for 24 h while a partial or complete degradation of MOF occurs for 24 h by increasing pH to 6.5 and 7.4, respectively. This is consistent with the previously reported degradation of these MIL-100(Fe) NPs in a highly concentrated aqueous phosphate solution at pH 7.4.[39]

**Biodegradability and internal distribution in macrophages**

In the next step, the cellular uptake of USPIO(20)@MIL by RAW 264.7 mouse macrophages was then investigated by combining confocal laser scanning microscopy (CLSM), TEM, and ICP-MS. For the CLSM

experiments, the fluorescent dye Rhodamine B (RhB) was encapsulated in the mesopores of USPIO(20)@MIL (see ESI for experimental details). Internalization of the RhB-labeled USPIO(20)@MIL nano-objects in the RAW 264.7 macrophages was clearly observed after an incubation time of 1 h (Fig. S16, ESI). The fluorescence intensity of the cells increased until 4 h while remaining constant for a longer incubation time. 2D TEM slices images of RAW 264.7 cells incubated with USPIO(20)@MIL NPs were recorded to characterize the internalization of USPIO(20)@MIL in RAW 264.7 cells, elucidate their intracellular distribution and fate over a period of one week.

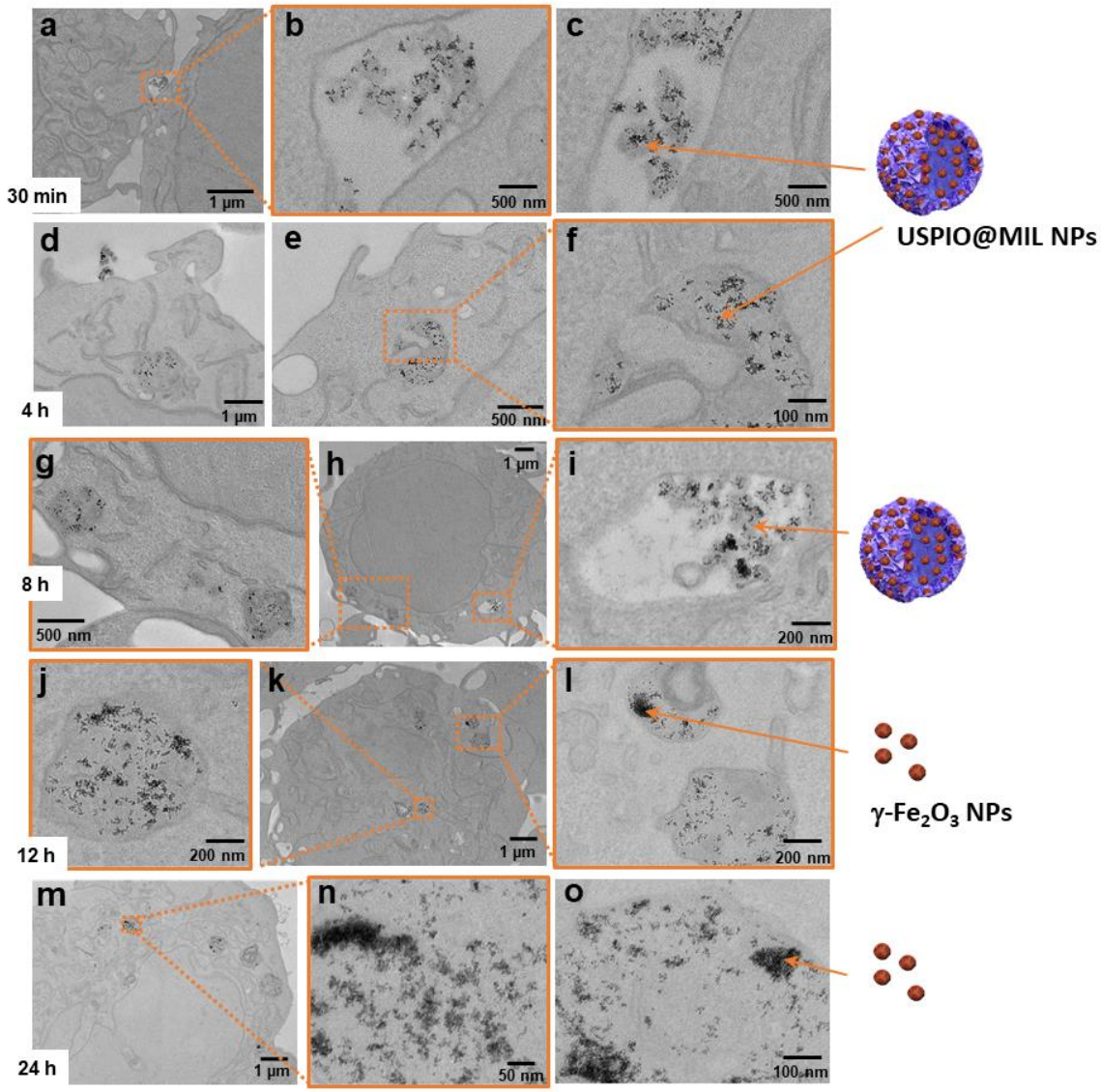


**Fig. 3** 2D TEM slices images of RAW 264.7 cells exposed to USPIO(20)@MIL (50 µg·mL$^{-1}$) in 2% FBS/DMEM medium for different incubation times (30 min, 4 hours, 8 hours, 12 hours and 24 hours).

As shown in Fig. 3a-c, after 30 min of incubation, USPIO(20)@MIL nano-object start to interact with the cell plasma membrane while a few nano-objects internalized into membrane-closed endosomes, without losing their bimodal nanostructure (small black dot and grey spheres in TEM images correspond respectively to $\gamma$-$Fe_2O_3$ and MIL-100(Fe) NPs). From 4 to 8 h (Fig. 3d-i), a large amount of USPIO(20)@MIL NPs is accumulated in endosomes. After 12 h of incubation (Fig. 3j-l), they start partially to degrade as revealed by the presence of individual $\gamma$-$Fe_2O_3$ NPs until their complete dissociation after an incubation time of 24 h (Fig. 3m-o). This is in agreement with the degradation of the outer MIL-100(Fe) shell of $Fe_3O_4$@C@MIL-100(Fe) in Hela cells as previously reported.[41] The degradation of MIL-100(Fe) is, as expected, due to the high intracellular concentration of phosphates and iron reductants such as glutathione. In the following days (Fig. S17, ESI), $\gamma$-$Fe_2O_3$ NPs are more concentrated in lysosomes and the density of $\gamma$-$Fe_2O_3$ NPs in the cytoplasm as well as endo/lysosomal compartments is significantly reduced after 5 days, suggesting their progressive degradation as previously observed for iron oxide NPs. This process is certainly involved in Fe recycling into ferritin proteins.[42] Overall, this two-stage degradation profile of USPIO(20)@MIL NPs clearly shows that these nano-objects are biodegradable after cell internalization. This is also associated with a high intracellular iron concentration, as shown by the quantification of the intracellular iron content by ICP-MS (Fig. S18, ESI). In agreement with CLSM experiments, a progressive increase of the $Fe^{3+}$ concentration is observed by increasing the incubation time until a plateau is reached after 6 h. Note that the evaluation of the biodegradability and intracellular fate of MOF based nanovectors as studied in the present article by TEM was rarely reported in literature.

**pH- and glutathione (GSH) responsive release properties of nano-objects**

For the development of USPIO(20)@MIL NPs as a theranostic nanocarrier, the drug-loading capacity and drug-release properties of MIL-100(Fe) need to be maintained after its assembly with USPIO. Interestingly, as shown by $N_2$ porosimetry, only a slight decrease in the BET area was observed with a value of 1460 ± 6 $m^2.g^{-1}$ for USPIO(20)@MIL, in comparison to that of pure MIL-100(Fe) NPs (1720 ± 6 $m^2.g^{-1}$), due to the presence of the dense non-porous USPIO (see Fig. 4b and S1, ESI). It indicates that the porosity of MIL-100(Fe) is kept once combined with maghemite NPs. The encapsulation of an active payload and its kinetics of delivery in PBS was then studied using Dox and MTX, selected due to their combined chemotherapeutic and anti-inflammatory properties (Fig. 4a).[1, 30-31, 43] Our objective was to develop a novel type of nanomedicine able to treat diseases with an inflammatory background such as cancer and auto-immune diseases. MTX was selected as this drug is not only the first-line conventional drug for RA but also one of the first generation anticancer drugs prescribed for human cancers.[1] Although clinical uses of MTX in cancer are well documented, its clinical efficacy can be limited due to its very short plasma half-life, poor pharmacokinetics, patient drug resistance, and eventually high dosages required for chemotherapy.[1, 24,44-45] Because of its broad-spectrum antitumor effect and low price, Dox is considered as one of the most effective chemotherapeutic agents, used as a first-line drug in numerous types of cancers.[46] However, Dox resistance often occurs in advanced tumors and this drug exhibits serious adverse effects, such as lethal cardiotoxicity.[46] If the vectorization of MTX and DOX has already been considered using a wide range of chemically different nanocarriers (liposomes, polymers, inorganic particles…),[45-46] these nanocarriers still suffered from many limitations in terms of large loadings and/or controlled release. In this work, the non toxic USPIO@MIL nano-objects have thus been considered as alternative nanocarriers of both MTX and Dox since the selective delivery of those drugs may achieve upregulated efficacy and safety. Note that different drug administration routes such as, oral, local, or intravenous delivery can be employed for anti-inflammatory nanomedicines.[1] While intravenous route enables a direct access to the whole body,

the local delivery of drug proved to be efficient, allowing to directly concentrate the drug into the inflamed tissue. If the choice of administration route depends on the location of the inflammation site, it relies also strongly on the nature of nanomedicine and its drug delivery properties. We have thus investigated the Dox and MTX loading capacity of USPIO(20)@MIL nano-object and its drug release properties in PBS. MTX was encapsulated in the porosity of both MIL-100(Fe) and USPIO(20)@MIL with a loading ratio of 60 and 47 wt%, respectively (Fig. S19 & S20, Table S2, ESI). This capacity is higher to that of MOFs previously reported.[47-50] Dox was encapsulated in MIL-100(Fe) and USPIO(20)@MIL with a loading of ~56 wt% and 50 wt% respectively (Fig. S22 and S23, Table S3, ESI), which exceeded most previously reported studies using either ZIF-8(Zn) (~4.9%) or MIL-101(Fe) (~13.4%) or Gd MOFs (~13.6%), except the mesoporous NU-1000(Zr) (~53.8%).[9, 51-54] Remarkably, this Dox loading capacity is significantly higher than the value of 14% reported for larger MIL-100(Fe) NPs (130 nm in diameter) previously synthesized by microwave assisted hydrothermal treatment.[18] The $N_2$ adsorption/desorption isotherms and the pore size distribution are fully consistent with the encapsulation of both drugs in USPIO(20)@MIL (see Fig. 4b and 4c). As shown by TEM, the drug loading did not affect the microstructure and morphology of both MIL-100(Fe) and USPIO(20)@MIL (see Fig. S20, ESI).

To achieve efficient drug delivery from the circulation to the target inflammatory tissues, the pH-responsiveness of release kinetics of MTX and Dox across neutral to acidic conditions was investigated. Indeed, endosomes (pH ~5-6) and lysosomes (pH ~4-5) of normal tissues as well as the synovial tissue of patient with RA are low-pH environments in comparison to blood (pH ~7.4).[55-56] Moreover, the affected joints of RA feature hypoxic microenvironment and increased level of glutathione (GSH, L-*γ*-glutamyl-L-cysteinylglycine), resulting from synovial proliferation, lymphocyte infiltration, and

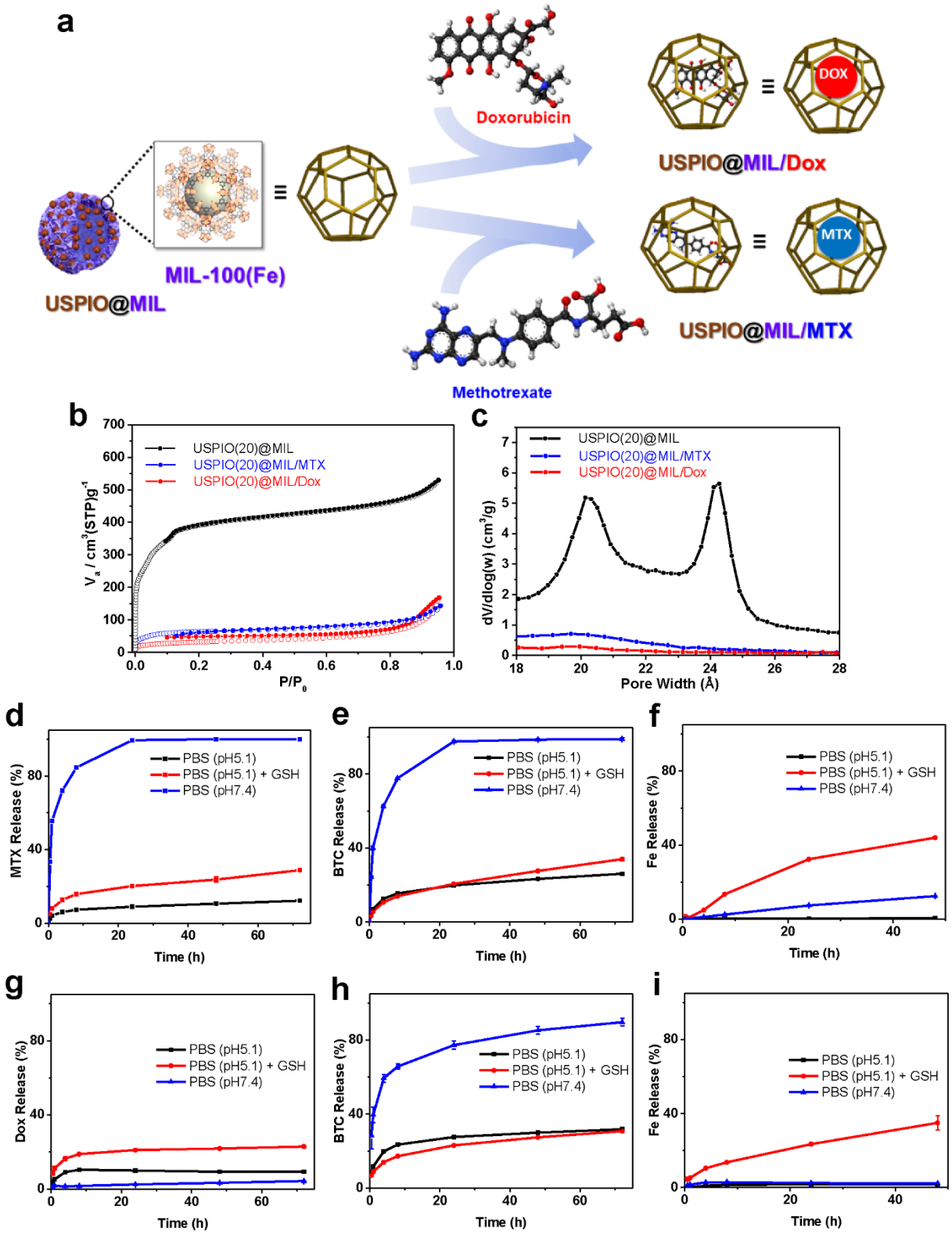


**Fig. 4.** a) Scheme of the doxorubicin and methotrexate loading in USPIO@MIL, (b) $N_2$ sorption isotherms and (c) pore size distribution (PSD) derived from the Barrett-Joyner-Halenda (BJH) pore size model of USPIO(20)@MIL, USPIO(20)@MIL/Dox, USPIO(20)@MIL/MTX, (d-f) MTX, BTC and Fe ions release from USPIO@MIL/MTX in different PBS media, (g-i) Dox, BTC and Fe ions release from USPIO@MIL/Dox in different PBS media. The experimental data were determined in triplicate.

neovascularization.[57-59] GSH is one of the important antioxidants present in the human body which protects cellular components from damage by free radicals.[57-60] Advantageously, the presence of GSH at high concentration (10 mM) and low pH in inflammatory joints can here be exploited as a stimulus to trigger the MTX and Dox release from USPIO(20)@MIL delivery system.

As shown in Fig. 4d,g, the release rate of MTX and Dox from USPIO(20)@MIL greatly depends on pH. A fast release of MTX from USPIO(20)@MIL is observed in PBS at pH 7.4 with drug release of 30, 70 and 85 % after 0.5, 4 and 8 h, respectively. The release of MTX is substantially slowed down at pH 5.1 in a medium containing PBS and GSH 10 mM (PBS/GSH) (Fig. 4d) mostly as a consequence of the slower kinetics of MOF degradation under more acidic conditions. The delivery profile of MTX follows two regimes: a fast release of about 17% of MTX in the first 8 h followed by a progressive one until reaching 30% of MTX released after 3 days. The fast release of MTX at pH 7.4 precludes the intravenous administration of USPIO(20)@MIL since MTX will be released in blood before USPIO(20)@MIL can reach the inflammatory cells. However, the local direct injection of USPIO(20)@MIL/MTX at the inflamed joint can be performed. In contrast, a minimal delivery of Dox from USPIO(20)@MIL was observed at pH 7.4 over 3 days (Fig. 4g) while in PBS/GSH medium at pH 5.1, it was slightly faster but kept progressive achieving a cumulative Dox delivery of about 20 % after 3 days. Since the internalization of USPIO(20)@MIL in RAW 264.7 cells occurs within the first 8h (Fig. 3), it means that the complete encapsulated Dox cargo can be administrated in the cells. This indicates that USPIO(20)@MIL/Dox could be administered either intravenously or locally at the inflamed joint.
To gain more insight in the release kinetics of MTX and Dox from USPIO(20)@MIL, we investigated the degradation kinetics of the MOF during the drug delivery process. The comparison between kinetics of Dox and MTX drug release and the degradation profiles of USPIO(20)@MIL (see Fig. 4d-i) suggests that the delivery process of both drugs is driven by the combined effects of diffusion from the pores and/or drug-matrix interactions as well as a partial degradation of MIL-100(Fe) in PBS[39], that occurs

more rapidly at pH 7.4 than 5.1. As shown by the quantification of 1,3,5-BTC and Fe released in the PBS media (Fig. 4e, f, h, i), MIL-100(Fe) degrades relatively fast at pH 7.4 due to the strong complexing ability of phosphate at this pH towards Fe cations. However, the Dox delivery is limited as the result of specific strong coordination bonds between hydroxy groups of Dox and coordinatively unsaturated Fe(III) sites of MIL-100(Fe) as previously demonstrated[61-62] while MTX is likely to exhibit only dispersive weak interactions with the MOF framework. Noteworthy, the high Fe release in the PBS/GSH medium at pH 5.1 indicates the complete degradation of MIL-100(Fe) that results from a chemical reduction of $Fe^{3+}$ centers by GSH as previously shown.[57-60, 63] Note that such high GSH levels are typically encountered in inflammatory diseases[64] which accelerates the degradation of the iron based USPIO(20)@MIL nano-object and thus triggers under acidic conditions the release of both Dox and MTX. The stimuli-responsive release properties of USPIO(20)@MIL/Dox can thus be exploited to selectively deliver Dox at the mildly acidic environment of inflamed joints.

**In vitro assays: cytotoxicity, anti-inflammatory and anti-cancer activity.**

In the next step, the *in vitro* cytotoxicity of USPIO(20)@MIL, USPIO(20)@MIL/MTX and USPIO(20)@MIL/Dox was assessed by a standard CCK-8 assay with different cell types (Hela tumor cells and RAW 264.7 cells) for an incubation time of 12 h and 24 h (see Experimental section for details). The viability of Hela cells exposed to USPIO(20)@MIL at a concentration of 20 and 50 $\mu g \cdot mL^{-1}$, was close to 92% and 91% after 12 h respectively and evolved slightly to 86% after 24 h (Fig. S25, ESI). Similar results were obtained with the bare MIL-100(Fe) NPs as previously shown.[18] These results show that both MIL-100(Fe) and USPIO(20)@MIL present a low cytotoxicity to Hela cells. Moreover, their cytotoxicity to RAW 264.7 cells is negligible since the viability of macrophages incubated with both NPs at 50 $\mu g \cdot mL^{-1}$ for 24 h is close to 80% (Fig. S26, ESI). The *in vitro* cytotoxicity of USPIO(20)@MIL/MTX and USPIO(20)@MIL/Dox was then evaluated exposing them to normal macrophages. RAW 264.7 were thus incubated with either USPIO(20)@MIL/MTX or free MTX for 24

h. The concentration of MTX (23 μg·mL$^{-1}$) was selected according to the MTX loading capacity of USPIO(20)@MIL. The cytotoxicity of USPIO(20)@MIL/MTX to normal macrophages is low since the viability of RAW 264.7 macrophages is close to 72% once exposed to USPIO(20)@MIL/MTX at a concentration of 50 μg·mL$^{-1}$ for 24 h (see Fig. 5b). In comparison, free MTX shows a high cytotoxic activity for normal macrophages decreasing cell viability to 34% at MTX concentration of 23 μg·mL$^{-1}$ which may be due to its robust dihydrofolate reductase inhibition activity to induce cell death as previously reported.[24] Similar results are obtained with USPIO(20)@MIL/Dox in comparison to free Dox. While a very high cytotoxicity is shown for the RAW 264.7 macrophages exposed to free Dox (2.5 to 25 μg·mL$^{-1}$), the RAW 264.7 viability is close to 100 % when incubated with USPIO(20)@MIL/Dox at the concentration of 5 to 50 μg·mL$^{-1}$ (see Fig. 5b and S27, ESI). Cell apoptosis assay by using calcein-AM/PI double staining was finally performed and confirms the low cytotoxicity of USPIO(20)@MIL/Dox and USPIO(20)@MIL/MTX to normal RAW 264.7 macrophages (Fig. S28, ESI).

To evaluate the anti-inflammation ability of the nanovectors, the RAW 264.7 macrophages were pretreated with lipopolysaccharide (LPS) for activation. Note that activated macrophages are involved in inflammatory diseases, including RA, lupus, inflammatory osteoarthritis, and cancer.[1, 24, 44, 65-66] They play an important role in RA, due to their abundance in inflamed synovial membrane and joints. RAW 264.7 cells activated by LPS spontaneously reveal an increased intracellular ROS level (Fig. S29, ESI). As reported previously, the magnitude of the inflammatory perturbation depends on the LPS concentration, that is known to increase the intracellular ROS level.[67] Once exposed to USPIO(20)@MIL and MIL-100(Fe) at 50 μg·mL$^{-1}$, the viability of activated RAW 264.7 cells decreases to a value of ~36% and ~38% after 24h of incubation (Fig. 5b, ESI). This shows that both USPIO(20)@MIL and MIL-100(Fe) nanovectors present a good anti-inflammatory efficacy associated to their fast internalization in macrophages and the high $Fe^{3+}$ intracellular concentration (Fig. S18, ESI). A similar phenomenon was previously reported for lipid-coated MIL-100(Fe) NPs whose internalization in different cell lines leads to their lysosomal degradation and iron delivery.[68] The high amount of

lysosomal iron induces a pyroptosis cell death mechanism which is an inflammatory form of programmed cell death.[69] The identification of the cell death mechanism in play with the toxicity of activated RAW 264.7 cells in the presence of USPIO(20)@MIL and MIL-100(Fe) is out of the scope of this study, and other cell death mechanisms induced by intracellular iron overexposure (ferroptosis) cannot be ruled out at this stage. However, it is worth noting that iron has been reported to trigger pyroptosis mediated by ROS that are produced in the presence of activated macrophages.[68, 70] Activated RAW 264.7 macrophages were further exposed to drug loaded nanovectors namely USPIO(20)@MIL/MTX and USPIO(20)@MIL/Dox. Notably, activated RAW 264.7 macrophages are much more sensitive to USPIO(20)@MIL/MTX than normal macrophages since the cell viability decreases to ~30% once incubated with the nano-objects at 50 $\mu g \cdot mL^{-1}$ for 24 h (Fig. 5b). This shows that USPIO(20)@MIL/MTX can induce a selective damage towards inflammatory macrophages. When compared with the free MTX alone, the USPIO(20)@MIL/MTX exhibited a significant higher anti-inflammatory efficiency since the viability of activated RAW 264.7 was almost 100% when exposed to free MTX at 23 $\mu g \cdot mL^{-1}$ for 24 h (Fig. 5b). The high efficiency of MTX formulated into USPIO(20)@MIL is certainly driven by the fast cellular internalization of USPIO(20)@MIL/MTX as previously shown. However, this anti-inflammatory activity is only slightly enhanced in comparison to USPIO(20)@MIL since the viability of activated RAW 264.7 exposed to USPIO(20)@MIL reached ~36% in the same conditions (50 $\mu g \cdot mL^{-1}$ with 24 h of incubation time). Such results can be explained by a significant delivery of MTX cargo from USPIO(20)@MIL in PBS prior to the nano-objects internalization. Activated macrophages were also exposed to USPIO(20)@MIL/Dox at 5, 20, 50 $\mu g \cdot mL^{-1}$ concentrations (Fig. S30, ESI) in DMEM medium (see Experimental section for details). They were also incubated with free Dox at 2.5, 10, 25 $\mu g \cdot mL^{-1}$ concentrations, which correspond to the amount of drug released from the nano-objects (at 5, 20, 50 $\mu g \cdot mL^{-1}$) respectively according to the release kinetics in PBS at 24 h (see above). When incubated with USPIO(20)@MIL/Dox at 5, 20, 50 $\mu g \cdot mL^{-1}$, cell viability decreased to ~89%, ~30%, and ~9%, respectively, in comparison with the non-treated cells. This cell viability is lower, for the two highest concentrations, than that obtained with USPIO(20)@MIL NPs for the same concentrations (*i.e.*

cell viability of ~88%, ~57%, and ~36% at 5, 20, 50 μg·mL$^{-1}$) thereby showing the superior cytotoxic capability of USPIO(20)@MIL/Dox on activated macrophages (Fig. S30, ESI). A strong decrease of the activated RAW 264.7 viability is also observed upon exposure to free Dox (*i.e.* cell viability of ~30%, ~18% and ~18% at 2.5, 10, 25 μg·mL$^{-1}$) but the free drug presents also a high cytotoxicity to normal macrophages even at very low concentration (2.5 μg·mL$^{-1}$) (Fig. 5b and S27, ESI). These results were confirmed by confocal microscopy. Activated RAW 264.7 macrophages were stained with calcein-AM/PI for discriminating living (green) cells and dead (red) cells. As shown in Fig. 5a, a large amount of dead cells are observed for activated RAW 264.7 macrophages exposed to USPIO(20)@MIL/Dox. The high efficiency of Dox formulated into USPIO(20)@MIL NPs is certainly driven by the high local drug accumulation in the cell as a result of the fast internalization of USPIO(20)@MIL NPs in the macrophages as well as the slow and progressive delivery of Dox in PBS (Fig. 4g).

To further confirm the anti-inflammatory capacity of the nanoformulations mentioned above, enzyme-linked immunosorbent assays (ELISA) were carried out to measure the concentrations of pro-inflammatory cytokines in cell culture media as crucial indexes of therapeutic efficacy. These cytokines including TNF-α, IL-1β, and IL-6 are crucial indicators for the pathological processes of RA.[65-66, 71] TNF-α is involved in the proliferation of synovial fibroblasts, activation of osteoblasts, and destruction of cartilage and bone. IL-1β induces cartilage metabolic disorder, bone absorption, and synovitis *via* promoting the release of other pro-inflammatory cytokines and proteinases while IL-6 is involved in activation of synovial fibroblasts and osteoblasts, leading to articular cartilage and bone erosion.[65-66, 71] Activated macrophages are exposed to drug formulations of low concentrations in order to prevent the cell apoptosis mediated expression of pro-inflammatory cytokines. As shown in Fig. 5c,d and Fig. S31 of ESI, the concentrations of the three pro-inflammatory cytokines, TNF-α, IL-1β, and IL-6, are remarkably increased in the cell culture medium of MIL-100(Fe) and USPIO(20)@MIL. For the free MTX, free Dox, MTX and Dox formulated in USPIO(20)@MIL NPs, the concentration of pro-inflammatory cytokines was decreased in different degrees.

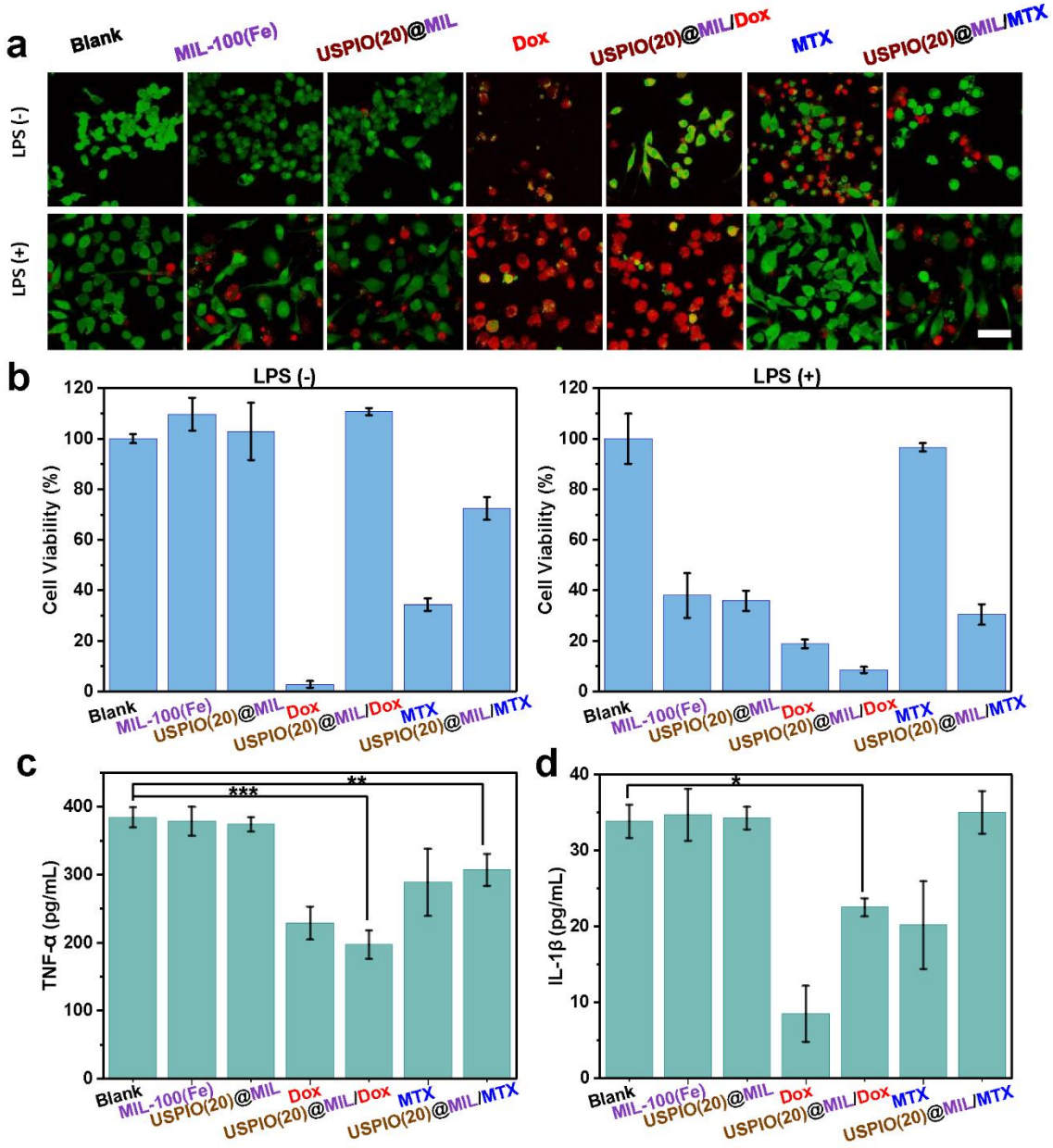


**Fig. 5** Anti-inflammatory properties of USPIO(20)@MIL/MTX and USPIO(20)@MIL/Dox. a) cell apoptosis assay by using calcein-AM/PI double staining of LPS (100 ng·mL$^{-1}$, 48 h) activated RAW 264.7 macrophages incubated with different drug formulations ([MIL-100(Fe)] = 40 μg·mL$^{-1}$, [USPIO(20)@MIL] = 50 μg·mL$^{-1}$, [Dox] = 25 μg·mL$^{-1}$, [USPIO(20)@MIL/Dox] = 50 μg·mL$^{-1}$, [MTX] = 23 μg·mL$^{-1}$, [USPIO(20)@MIL/MTX] = 50 μg·mL$^{-1}$) for 24 h. For the representative images of (a), activated RAW 264.7 macrophages were stained with calcein-AM/PI for discriminating living (green) and dead (red) cells (scale bar = 50 μm). b) Cell viability assay by using CCK-8 staining of normal RAW 264.7 macrophages and LPS activated RAW 264.7 macrophages incubated with aforementioned drug formulations. c-d) The concentrations of the inflammatory cytokines (c) TNF-α and (d) IL-1β in cell culture media after the treatment of different formulations ([MIL-100(Fe)] = 4 μg·mL$^{-1}$, [USPIO(20)@MIL] = 5 μg·mL$^{-1}$, [Dox] = 0.25 μg·mL$^{-1}$, [USPIO(20)@MIL/Dox] = 5 μg·mL$^{-1}$, [MTX] = 2.3 μg·mL$^{-1}$, [USPIO(20)@MIL/MTX] = 5 μg·mL$^{-1}$) for 24 h. Note that the concentration of Dox here was ten times lower than the loaded Dox of USPIO(20)@MIL/Dox to limit its toxicity. Results are shown as mean ± SD, n = 3. *P < 0.05, **P < 0.01, ***P <0.001. The experimental data were performed in triplicate.

In all cases a strong inhibition of IL-1β and TNF-α secretion was observed while the expression of IL-6 was moderately decreased. In contrast, USPIO(20)@MIL/MTX was mainly efficient to reduce the serum concentration of TNF-α. These results thus showed that USPIO(20)@MIL/Dox is prone to inhibit synovitis in the affected joints and also protect articular cartilage and bone against erosion and destruction due to its remarkable ability to reduce the production of pro-inflammatory cytokines.

Finally, the anti-cancer activity of USPIO(20)@MIL/Dox was evaluated by CCK-8 staining kit and confocal microscopy. The cell internalization process as monitored by confocal microscopy with time (Fig. S32, ESI) was achieved in the first 8h of incubation. In the presence of USPIO(20)@MIL/Dox at 50 $\mu g \cdot mL^{-1}$, the viability of cancer Hela cells decreases to 8% (Fig. 6b). When compared to the viability of Hela cells exposed to free Dox (25% at 25 $\mu g \cdot mL^{-1}$), the USPIO(20)@MIL/Dox nano-object exhibited a higher anti-cancer efficiency as previously shown for surface decorated MIL/USPIO-cit nano-object (Fig. 6).[18] This high efficacy is certainly induced by the fast internalization of nano-objects in the cancer cells and thus the subsequent intracellular drug accumulation. Furthermore, the encapsulation of Dox into nano-objects might overcome the resistance to Dox treatment that occurs in tumor cells as a result of the expression of P-glycoprotein (P-gp), which pumps out the drug from the cells.[72]

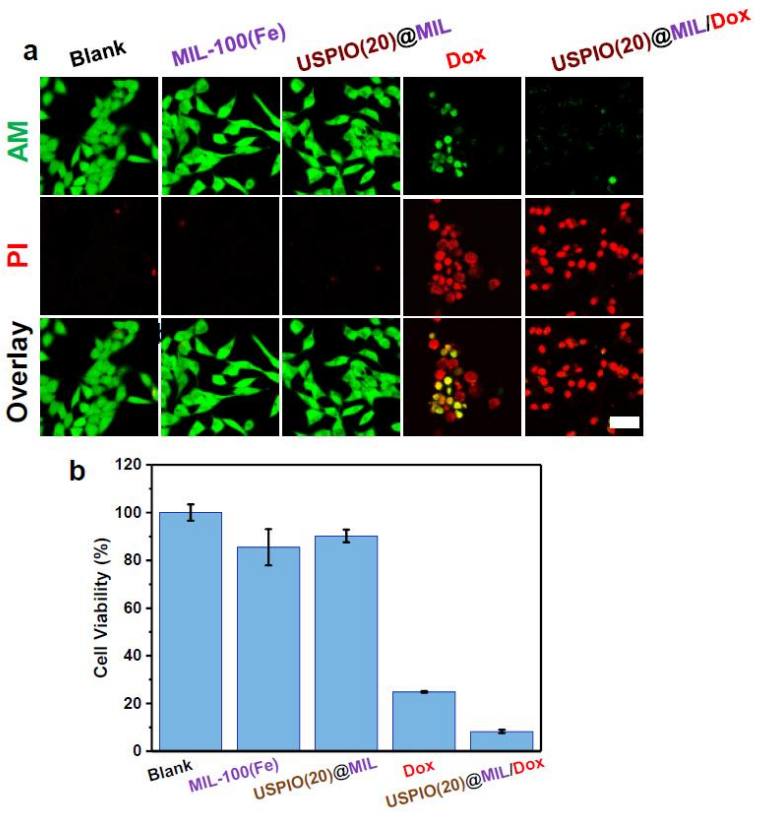


**Fig. 6** a) AM/PI staining and (b) Cell viability of Hela cells incubated for 24 h with MIL-100(Fe), USPIO(20)@MIL, Dox and USPIO(20)@MIL/Dox at the concentrations of 40, 50, 25 and 50 µg·mL$^{-1}$, respectively. Scale bar = 50 µm for (a). The experimental data were performed in triplicate.

**Relaxometric properties of nano-objects, *in vivo* MRI experiments**

In the final step, we have evaluated the performance of USPIO(20)@MIL as $T_2$ MRI contrast agent due to the presence of γ-$Fe_2O_3$ NPs. As shown in Fig. 7a, USPIO(20)@MIL could be easily separated using an external magnetic field, which suggests its excellent magnetic properties. For their potential use as MRI contrast agents, the $r_2$ relaxivity of USPIO(20)@MIL was assessed in PBS/BSA medium by measuring the $T_2$ (transverse) relaxation times of proton spins for different iron concentrations at 4.7 T (Fig. 7b). As expected, pure maghemite nanoparticles exhibit the highest value of $r_2$ (171 mM$^{-1}$·s$^{-1}$) in the same range of magnitude as commercial iron oxide contrast agents such as Endorem® or Sinerem®.[73-74] Noteworthy, by combining MIL-100(Fe) NPs with 20 wt% of USPIO, the $r_2$ value of ~93 mM$^{-1}$·s$^{-1}$ is about 30 times higher than that of MIL-100(Fe) and comparable to the commercial

Endorem® and Sinerem® (Table S4). Notably, the $r_2$ value of USPIO(10)@MIL (*i.e.* 38 $mM^{-1}\cdot s^{-1}$) is lower, due to the smaller amount of $\gamma$-$Fe_2O_3$ relative to the total iron concentration. These results show that the relaxometric properties of these nano-objects can be finely tuned upon varying the maghemite content. With the exception of $Fe_3O_4$-ZIF-8,[75] $Fe_3O_4$@C@MIL-100(Fe)[41] and MIL-101(Fe)-$NH_2$/USPIO,[76] the $r_2$ value is higher to the previously reported magnetic based MOF NPs or comparable to the surface decorated MIL/USPIO-cit(10).[18] Note also that $Fe_3O_4$@C@MIL-100(Fe) NPs exhibit a poor crystallinity and low porosity ($S_{BET}$ = 109 $m^2\cdot g^{-1}$), suggesting that the MOF exhibits an amorphous character. Moreover, the low stability of ZIF-8 NPs in water and aqueous phosphate solutions is a critical issue for the biomedical application of $Fe_3O_4$-ZIF-8 due to detrimental $Zn^{2+}$ ion burst release or toxicity effects. The high relaxivity of USPIO(20)@MIL is certainly related to the magnetic properties of USPIO(20)@MIL since the relaxivity rate ($r_2$) of a $T_2$-MRI contrast agent is proportional to the square of the saturation magnetization ($M_{sat}$). As shown by vibrating sample magnetometry (VSM) (see ESI for experimental details and Fig. S33, ESI), the USPIO(20)@MIL nano-objects present a superparamagnetic behaviour characteristic of maghemite NPs. The magnetization curve of USPIO(20)@MIL was fitted by the Langevin model, considering maghemite NPs with a diameter of ~6 nm. Note that some of us have previously fully characterized the magnetic properties of bare γ-$Fe_2O_3$ NPs used in this study.[18] Noteworthy, as shown in Table S5, the values of saturation magnetization of USPIO(20)@MIL and USPIO(10)@MIL (*i.e.* 68 and 71 $Am^2\cdot kg^{-1}$ respectively) are fully consistent with those previously reported for USPIO. Interestingly, these values are significantly higher than those of most porous magnetic MOFs-based composites previously reported (see Table S5). Encouraged by their good relaxometric properties, $T_2$-weighted MRI of USPIO(20)@MIL was further evaluated *in vivo*. 90 µL of USPIO(20)@MIL at 10 $mg\cdot mL^{-1}$ in PBS/BSA (5.4% w/v) medium corresponding to a concentration of ~250 µmol Fe/kg, was injected in the mouse tail vein and MR images were recorded before and just after USPIO(20)@MIL injection. In Fig. 7c, an homogenous decrease of signal was observed in the mouse liver and spleen right after the contrast agent injection on the T2*-weighted images. For example, in the liver, the contrast agent generated a 56% decrease of signal-to-noise ratio

($\Delta SNR = SNR_{before} - SNR_{after} = 19.4 - 8.5 = 10.9$) due to the high $T_2$* effect. These results demonstrate that USPIO(20)@MIL can be used as a highly performing $T_2$ MRI contrast agent.

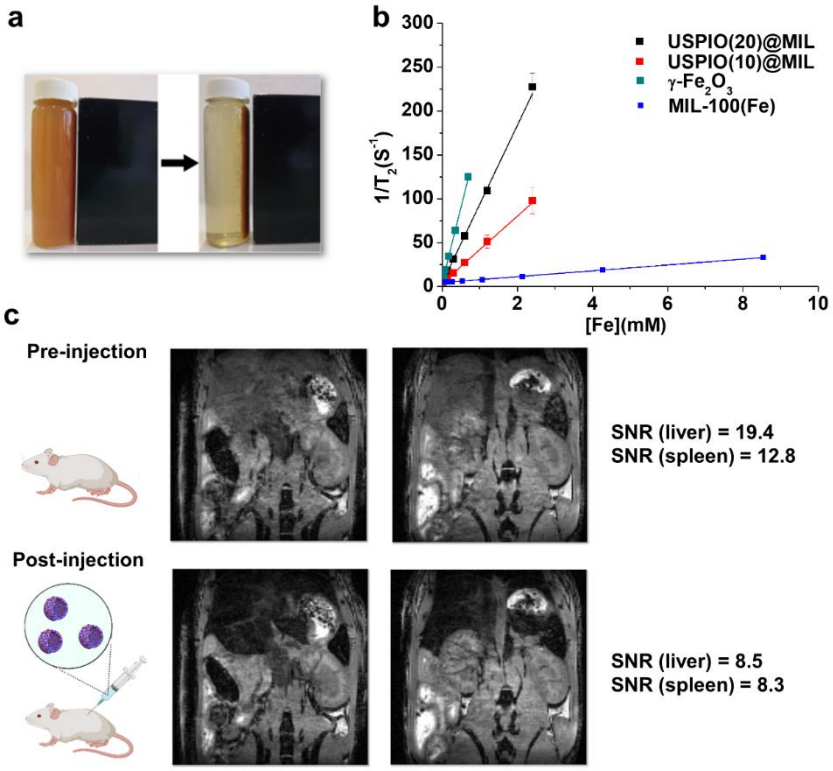


**Fig. 7.** a) photograph showing the separation of USPIO(20)@MIL from aqueous solution under an external magnetic field; b) Transverse relaxation rates ($1/T_2$, $s^{-1}$) as a function of iron concentration for $\gamma$-$Fe_2O_3$, MIL-100(Fe) and USPIO(X)@MIL (X=10 & 20) prepared in PBS/BSA solution at pH 7.5; c) T2*-weighted gradient echo images of the mouse abdomen before and after injection of contrast agent USPIO(20)@MIL.

## CONCLUSIONS

In conclusion, we report the design of a novel hybrid nano-object coupling MIL-100(Fe) and maghemite NPs that was prepared through a direct cost-effective and reliable green protocol at RT. According to TEM and electron tomography, the hierarchical nanostructure of these nano-objects consists of maghemite NPs located either at the surface or embedded in the core of MIL-100(Fe) NPs. We have shown that the synergistic combination of the physico-chemical of both NPs associated to the encapsulation of two complementary drugs (Dox and MTX) could be fully exploited to create a multifunctional theranostic platform for the therapy of inflammatory diseases. This nanovector

exhibits an excellent colloidal stability under simulated intravenous conditions, low cytotoxicity and an extremely high Dox and MTX loading efficacy. Their pH- and GSH responsive Dox/MTX release properties are mainly driven by an interplay between drug/MOF interactions and the biodegradability of MOFs, as revealed by the complete characterization of their internalization, intracellular distribution and fate in macrophages by CLSM and TEM. Remarkably, USPIO(20)@MIL/Dox and USPIO(20)@MIL/MTX nanovectors present an excellent anti-inflammatory efficacy ascribed to their high toxicity directed towards activated macrophages and their ability to reduce the secretion of inflammatory cytokines. Moreover, USPIO(20)@MIL/Dox exhibits a high anti-tumoral activity associated to the progressive delivery of its encapsulated Dox cargo to the cancer cells. Therefore, USPIO(20)@MIL/Dox can be considered as a dual-targeting therapeutic strategy, inhibiting tumor growth and reducing the inflammation. Finally the USPIO(20)@MIL nanovectors exhibits a superparamagnetic behavior inherent in the presence of maghemite NPs and thus can be used as $T_2$ MRI contrast agents for theranostics. This work has numerous perspectives depending on the choice of the MOF and magnetic nanoparticles. In particular, the use of magnetic iron based particles with other chemical composition and particle diameter can pave the way towards the design of hierarchical nano-objects combining multimodal imaging and therapeutics (magnetic targeting, magnetic fluid hyperthermia).

## EXPERIMENTAL

### TEM of cells

All chemicals were used as received without any further purification: glutaraldehyde solution 25% (Sigma-Aldrich), sodium cacodylate trihydrate (Sigma-Aldrich, ≥ 98%). RAW 264.7 cells were seeded into a 6-well plate at $2\times10^5$ cells per well in 2 mL of complete medium, and cultured in a 5% $CO_2$ atmosphere at 37 °C overnight. The culture medium was then replaced with 2 mL of complete medium

containing USPIO(20)@MIL at a concentration of 50 μg·mL$^{-1}$ for 30 min, 4 h, 8 h, 12 h and 24 h and after washing with PBS were maintained in 2% FBS supplemented DMEM medium for 1, 2, 5, and 8 days at 37 °C. After certain intervals, the medium was removed and cells were firstly washed twice with PBS and once with 0.2 M Na cacodylate buffer pH 7.2, and then fixed with 2% glutaraldehyde in 0.1 M Na cacodylate buffer pH 7.2, for 1 hour at room temperature. Samples were then contrasted with Oolong Tea Extract (OTE) 0.5% in cacodylate buffer, postfixed with 1% osmium tetroxide containing 1.5% potassium cyanoferrate, gradually dehydrated in ethanol (30% to 100%) and substituted gradually in mix of ethanol-epon and embedded in Epon. (Delta microscopie – France). Thin sections (80 nm) were collected onto 200 mesh copper grids. Grids were examined with Hitachi HT7700 electron microscope operated at 80 kV (Elexience – France), and images were acquired with a charge-coupled device camera (AMT).

***In vitro* cytotoxicity assay of USPIO(20)@MIL and MIL-100(Fe) against Hela cells and normal RAW 264.7 cells**

Hela cells in logarithmic phase were rinsed twice in PBS and then treated with 1 mL Trypsin to form $10^5$/mL cells suspension. 100 μL Hela cells suspension were seeded in 96-well plates ($10^4$/well) and incubated overnight. Then, MIL-100(Fe) or USPIO(20)@MIL in DMEM/FBS at different concentrations (10, 20, 50, 100 and 200 μg·mL$^{-1}$) was added to each well, incubated for 12 or 24 hours at 37 °C and under 5% of $CO_2$. 10 μL CCK-8/well were added to the cells and after incubation for further 2 hours, 96-well plate was transferred into a microplate reader (excitation at 450 nm) for UV-Vis absorbance analysis. The resulting UV-Vis absorbance values were normalized to the UV-Vis absorbance signals value of the control groups. All the experimental points were assessed three times, with error bars representing standard error of the mean. The cell cytotoxicity of MTX was further studied on RAW 264.7 cells, following the same protocol.

Cell survival rate (%) = $[(A_{\text{Experimental group}} - A_{\text{blank group}}) / (A_{\text{Control group}} - A_{\text{blank group}})] \times 100\%$

***In vitro* cytotoxicity assay of USPIO(20)@MIL/MTX and USPIO(20)@MIL/Dox against normal RAW 264.7 cells**

RAW 264.7 cells were seeded into a 96-well plate at a density of $1 \times 10^4$ cells per well and allowed to adhere overnight. The *in vitro* cytotoxicity of RAW 264.7 cells after incubation for 24 h with MIL-100(Fe) (40 $\mu g \cdot mL^{-1}$), USPIO(20)@MIL (50 $\mu g \cdot mL^{-1}$), USPIO(20)@MIL/MTX with equivalent free MTX at 23 $\mu g \cdot mL^{-1}$ and USPIO(20)@MIL/Dox with equivalent free Dox at 25 $\mu g \cdot mL^{-1}$ was evaluated in triplicate as previously described. Meanwhile, different concentrations of USPIO(20)@MIL/Dox (5, 10, 20, 50 and 100 $\mu g \cdot mL^{-1}$) and equivalent free Dox (2.5, 5, 10, 25 and 50 $\mu g \cdot mL^{-1}$) were also studied on RAW 264.7 cells. To visualize the toxicity effects to normal RAW 264.7 cells, the staining of Live & Dead cells was performed by calcein AM/PI co-staining and observed at 488 and 543 nm. Calcein AM is a hydrophobic compound, which passes easily through cell membranes into live cells and is used for cell viability assays and PI is membrane impermeant and generally excluded from viable cells, which is commonly used for identifying dead cells. First, RAW 264.7 cells were seeded into 35 mm confocal dishes at a density of $1 \times 10^4$ cells per dish and after the treatment of different formula ([MIL-100(Fe)] = 40 $\mu g \cdot mL^{-1}$, [USPIO(20)@MIL] = 50 $\mu g \cdot mL^{-1}$, [Dox] = 25 $\mu g \cdot mL^{-1}$, [USPIO(20)@MIL/Dox] = 50 $\mu g \cdot mL^{-1}$, [MTX] = 23 $\mu g \cdot mL^{-1}$ and [USPIO(20)@MIL/MTX] = 50 $\mu g \cdot mL^{-1}$). The cells were stained by AM/PI (dilution ×1000) containing DMEM for 15 min and then washed with PBS for confocal imaging.

**Anti-inflammatory capacity of USPIO(20)@MIL/MTX and USPIO(20)@MIL/Dox**

To investigate the anti-inflammatory capacity of MTX or Dox loaded USPIO(20)@MIL, RAW 264.7 cells were first activated by lipopolysaccharide (LPS). To verify the successful construction of inflammatory model, intracellular reactive oxygen species (ROS) production was detected by dichlorofluorescein diacetate (DCF-DA) probe. DCF-DA could be oxidized to green fluorescent-dichlorofluorescein by intracellular ROS. Thus, the fluorescence intensity could indicate the levels of ROS in the cells. RAW

264.7 cells were seeded at a density of $1 \times 10^5$ cells/mL into a confocal dish and incubated at 37 °C under 5% $CO_2$ overnight. Then, the cells were incubated with LPS at a concentration of 100 ng·mL$^{-1}$ for 48 h. The media was replaced with 2 mL serum-free medium containing DCF-DA (10 μM) and cultured for 30 min in dark. The nucleus was stained by Hoechst. After washing with PBS, a confocal laser microscope was used for ROS imaging at an excitation wavelength of 488 nm.

After this activation step, the DMEM medium was replaced by a fresh DMEM medium containing MIL-100 (Fe), USPIO(20)@MIL, and USPIO(20)@MIL/MTX at a concentration of 40, 50 and 50 μg·mL$^{-1}$, respectively. For comparison, activated RAW 264.7 cells were exposed to free MTX at a concentration of 23 μg·mL$^{-1}$. After 24 h incubation, 10 μL CCK-8 was added to each well and after incubation for further 2 hours, the 96-well plate was transferred into a microplate reader (excitation at 450 nm) for UV-Vis absorbance analysis. Then, the anti-inflammatory capacity of Dox loaded USPIO(20)@MIL was also investigated. After the same activation step, the DMEM medium was replaced by a fresh DMEM medium containing USPIO(20)@MIL and USPIO(20)@MIL/Dox at a concentration of 5, 20 or 50 μg·mL$^{-1}$. For comparison, activated RAW 264.7 cells were exposed to free Dox at a concentration of 25 μg·mL$^{-1}$. To visualize the inhibition effects of activated RAW 264.7 cells, RAW 264.7 cells were seeded into confocal dishes, followed by similar treatment for AM/PI staining. The anti-inflammatory capacity of each group was evaluated in triplicate.

**Evaluation of the concentrations of pro-inflammatory cytokines by enzyme-linked immunosorbent assay (ELISA) assays**

In comparison to previous experiments, the concentrations of formulations were 10 times lower in order to maintain a cell viability higher than 80%. RAW 264.7 cells were first seeded into 12-well plate at a density of $1 \times 10^5$ cells/mL and after the step of LPS activation, cells were further treated with different formulations ([MIL-100(Fe)] = 4 μg·mL$^{-1}$, [USPIO(20)@MIL] = 5 μg·mL$^{-1}$, [Dox] = 0.25 μg·mL$^{-1}$ (100 times lower), [USPIO(20)@MIL/Dox] = 5 μg·mL$^{-1}$, [MTX] = 2.3 μg·mL$^{-1}$, [USPIO(20)@MIL/MTX] = 5 μg·mL$^{-1}$) for 24 h, and each group was prepared in triplicate. Then, the supernatant was collected and

centrifuged to remove cells pellets and materials for next step detection. Briefly, mouse tumor necrosis factor alpha (TNF-α) DY410 DuoSet® ELISA, R&D Systems; mouse Interleukin 1 beta (IL-1β) DY401 DuoSet® ELISA, R&D Systems; mouse interleukin 6 (IL-6) DY406 DuoSet ELISA, R&D Systems were used to access TNF-α, IL-1β, and IL-6 concentrations from cell culture media samples by the standard ELISA technique, namely sandwich ELISAs (Capture antibody + sample or standard + Detection antibody). Following the manufacturer's instructions, the samples were finally diluted by five times for ELISA assays based on absorbance values of the recombinant mouse standard.

**Cytotoxicity of USPIO(20)@MIL/Dox against Hela cells**

First, the cellular uptake of the USPIO(20)@MIL/Dox was evaluated by CLSM on Hela cells. Cells were seeded into confocal dishes ($2 \times 10^5$ cells per dish) and maintained overnight. The medium was then replaced with 2 mL of complete medium containing USPIO(20)@MIL/Dox (50 μg/mL), followed by an incubation at 37°C for 1 h, 2 h, 4 h, 6 h and 8 h. Then cells were washed with PBS for three times to remove the residual media and stained by Hoechst (dilution ×5000) for 15 min. Then the as prepared samples were imaged by CLSM (ZEISS LSM780, Germany). The laser excitation wavelength of Hoechst and Dox was 405 nm and 488 nm, respectively. Hela cells were seeded into a 96-well plate at a density of $1 \times 10^4$ cells per well and allowed to adhere overnight. Then, different formula were added to each well, including control groups such as MIL-100(Fe) (40 $\mu g \cdot mL^{-1}$), USPIO(20)@MIL (50 $\mu g \cdot mL^{-1}$) and equivalent free Dox (25 $\mu g \cdot mL^{-1}$) as well as experimental groups USPIO(20)@MIL/Dox at a concentration of 50 $\mu g \cdot mL^{-1}$. After 24 h, 10 μL CCK-8 were added to each well and after incubation for further 2 hours, 96-well plate was transferred into a microplate reader (excitation at 450 nm) for UV-Vis absorbance analysis. Similarly, the therapeutic effects of the USPIO(20)@MIL/Dox was also evaluated through AM/PI staining by CLSM on Hela cells. Hela cells were seeded into 35 mm confocal dishes at a density of $1 \times 10^4$ cells per dish and after the treatment of different formula, the cells were stained by AM/PI (dilution ×1000) containing DMEM for 15 min and then washed with PBS for confocal

imaging. The laser excitation wavelength of AM and PI was 488 nm and 543 nm, respectively. The cytotoxicity of each group against Hela cells was evaluated in triplicate.

***In vivo* MRI experiments**

All animal experimental protocols were approved by the Animal Care and Use Institutional Ethics Committee of Bordeaux, France (Approval No. 5012032-A). *In vivo* experiments were performed on a 7T Bruker Biospec System equipped with a gradient system capable of 660 mT/m maximum strength and 110-µs rise time. A volume resonator (86 mm inner diameter, active length = 70 mm) operating in quadrature mode was used for excitation, and a four-element phased array coil (total outer dimensions: 30 × 25 $mm^2$) was used for signal reception. Balb/C mice (23-25 g) were purchased from a commercial breeder (Charles River, Paris, France). Mice were anesthetized with isoflurane (1.0-1.5% in air). The animals were positioned within the magnet with the liver placed at the center of the MR coil. A bolus of 90 µL of the sample was injected in the mouse tail vein while inside the magnet after the acquisition of pre-contrast $T_2$*-weighted and $T_1$-weighted acquisitions. The sample consists of USPIO(20)@MIL at 12 $mg \cdot mL^{-1}$ in PBS-BSA media (PBS 0.01 mol/L + BSA 5.4% w/v). This corresponds to a concentration of ~250 µmol Fe/kg which is typically used for in vivo MRI by using USPIO contrast agents. A 3D gradient echo $T_2$*-weighted sequence was performed before (pre-contrast) and after (post-contrast) contrast agent injection with the following parameters: TE/TR = 2/12 ms; flip angle: 15°; Field-Of-View: 35 × 25 × 22 mm; Matrix: 128 × 128 × 64; spatial resolution: 273 × 195 × 343 µm. Number of excitations: 2; total acquisition time: 3 min 16 sec. A 3D $T_1$-weighted Ultra-Short Echo time (UTE) sequence was performed before and after contrast agent injection with the following parameters: TE/TR = 0.031/5 ms; flip angle: 30°; Field-Of-View: 35 × 35 × 35 mm; Matrix: 128 × 128 × 128; spatial resolution: 273 × 273 × 273 µm; number of spokes: 51360; total acquisition time: 4 min 16 sec.

## Authors contributions

H. Z. and S. S. optimized the synthesis and structural characterization of nano-objects under the supervision of N. S., E. D. and N. G. F. D. and C. S. optimized the RT synthesis of MIL-100(Fe). H. Z. and A. M. optimized the drug encapsulation and the colloidal stability of nano-objects under the supervision of C. S and N. S. S. M. (CRMSB) performed the relaxivity experiments and the in vivo MRI experiments. N. M. performed the TEM and HAADF STEM experiments. D. I. and O. E. performed the electron tomography experiments. H. Z., C. P. and F. C studied the internalization of nano-objects in macrophages by TEM. J. S. characterized the magnetic properties of the nano-objects. J. M. G. characterized the nano-objects by $^{57}$Fe Mössbauer spectrometry. H. Z. performed all the experiments that evaluate the cytotoxicity, anti-cancer and anti-inflammation capacity of nano-objects under the supervision of F. G., S. M. (Institut Galien), N. S. and C. S. N. S. wrote the article with the contribution and help of all authors.

## Conflicts of interest

There are no conflicts to declare.

## Acknowledgements

H.Z. is grateful for the support from CSC grant (grant number 201808320434). The authors acknowledge Nicolas Tsapis (Institut Galien, Université paris-saclay) for fruitful discussions. This work has benefited from the facilities and expertise of MIMA2 MET – GABI, INRA, Agroparistech, 78352 Jouy-en-Josas, France. MIMA2: https://doi.org/10.15454/1.5572348210007727E12.

## References

1 R. Brusini, M. Varna, P. Couvreur, Advanced Nanomedicines for the Treatment of Inflammatory Diseases, *Adv. Drug Deliv. Rev.,* 2020, **157**, 161-178.

2 R. Molinaro, C. Corbo, M. Livingston, M. Evangelopoulos, A. Parodi, C. Boada, M. Agostini, E. Tasciotti, Inflammation and Cancer: In Medio Stat Nano, *Curr. Med. Chem.,* 2018, **25**, 4208-4223.
3 S. Hua, M. B. C. de Matos, J. M. Metselaar, G. Storm, Current Trends and Challenges in the Clinical Translation of Nanoparticulate Nanomedicines: Pathways for Translational Development and Commercialization, *Front. Pharmacol.,* 2018, **9**, 790.
4 P. Horcajada, R. Gref, T. Baati, P. K. Allan, G. Maurin, P. Couvreur, G. Ferey, R. E. Morris, C. Serre, Metal-Organic Frameworks in Biomedicine, *Chem. Rev.,* 2012, **112**, 1232-1268.
5 K. Lu, T. Aung, N. Guo, R. Weichselbaum, W. Lin, Nanoscale Metal-Organic Frameworks for Therapeutic, Imaging, and Sensing Applications, *Adv. Mater.,* 2018, **30**, 1707634.
6 L. Wang, M. Zheng, Z. Xie, Nanoscale Metal-Organic Frameworks for Drug Delivery: A Conventional Platform with New Promise, *J. Mater. Chem. B,* 2018, **6**, 707-717.
7 M. -X. Wu, Y. -W. Yang, Metal-Organic Framework (MOF)-Based Drug/Cargo Delivery and Cancer Therapy., *Adv. Mater.,* 2017, **29***,* 1606134.
8 I. Abánades Lázaro, R. S. Forgan, Application of Zirconium MOFs in Drug Delivery and Biomedicine, *Coord. Chem. Rev.,* 2019, **380**, 230-259.
9 P. Horcajada, T. Chalati, C. Serre, B. Gillet, C. Sebrie, T. Baati, J. F. Eubank, D. Heurtaux, P. Clayette, C. Kreuz, J. S. Chang, Y. K. Hwang, V. Marsaud, P. N. Bories, L. Cynober, S. Gil, G. Ferey, P. Couvreur, R. Gref, Porous Metal-Organic-Framework Nanoscale Carriers as a Potential Platform for Drug Delivery and Imaging, *Nat. Mater.,* 2010, **9**, 172-178*.*
10 W. Cai, C. -C. Chu, G. Liu, Y. -X. Wang, Metal-Organic Framework-Based Nanomedicine Platforms for Drug Delivery and Molecular Imaging, *Small,* 2015, **11**, 4806-4822.
11 F. D. Duman, R. S. Forgan, Applications of Nanoscale Metal-Organic Frameworks as Imaging Agents in Biology and Medicine, *J. Mater. Chem. B,* 2021, **9**, 3423-3449.
12 J. W. M. Osterrieth, D. Fairen-Jimenez, Metal-Organic Framework Composites for Theragnostics and Drug Delivery Applications, *Biotechnol. J.,* 2021, **16**, 2000005.
13 W. Zhu, J. Zhao, Q. Chen, Z. Liu, Nanoscale Metal-Organic Frameworks and Coordination Polymers as Theranostic Platforms for Cancer Treatment, *Coord. Chem. Rev.,* 2019, **398**, 113009.
14 H. Zhao, C. Serre, E. Dumas, N. Steunou, in *Metal-Organic Frameworks for Biomedical Applications,* ed. M. Mozafari, Elsevier, 2020, Chapter 18 , 397-423.
15 M. Peller, K. Böll, A. Zimpel, S. Wuttke, Metal–Organic Framework Nanoparticles for Magnetic Resonance Imaging, *Inorg. Chem. Front.,* **2018**, *5*, 1760-1779.
16 H. Zhang, Y. Shang, Y. -H. Li, S. -K. Sun, X. -B. Yin, Smart Metal-Organic Frameworks-Based Nanoplatforms for Imaging-Guided Precise Chemotherapy, *ACS Appl. Mater. Interfaces,* 2019, **11**, 1886-1895.
17 R. Ettlinger, N. Moreno, N. Ziółkowska, A. Ullrich, H. -A. Krug von Nidda, D. Jirák, K. Kerl, H. Bunzen, *In Vitro* Studies of $Fe_3O_4$ -ZIF-8 Core-Shell Nanoparticles Designed as Potential Theragnostics, *Part. Part. Syst. Charact.,* 2020, **37**, 2000185.
18 S. Sene, M. T. Marcos-Almaraz, N. Menguy, J. Scola, J. Volatron, R. Rouland, J.-M. Grenèche, S. Miraux, C. Menet, N. Guillou, F. Gazeau, C. Serre, P. Horcajada, N. Steunou, Maghemite-nanoMIL-100(Fe) Bimodal Nanovector as a Platform for Image-Guided Therapy, *Chem,* 2017, **3**, 303-322.
19 J. Liu, J. Huang, L. Zhang, J. Lei, Multifunctional Metal-Organic Framework Heterostructures for Enhanced Cancer Therapy, *Chem. Soc. Rev.,* 2021, **50**, 1188-1218.
20 M. d. J. Velásquez-Hernández, M. Linares-Moreau, E. Astria, F. Carraro, M. Z. Alyami, N. M. Khashab, C. J. Sumby, C. J. Doonan, P. Falcaro, Towards Applications of Bioentities@MOFs in Biomedicine, *Coord. Chem. Rev.,* 2021, **429**, 213651.
21 E. Bellido, T. Hidalgo, M. V. Lozano, M. Guillevic, R. Simon-Vazquez, M. J. Santander-Ortega, A. Gonzalez-Fernandez, C. Serre, M. J. Alonso, P. Horcajada, Heparin-Engineered Mesoporous Iron Metal-Organic Framework Nanoparticles: Toward Stealth Drug Nanocarriers, *Adv. Healthcar. Mater.,* 2015, **4**, 1246-1257.
22 V. Agostoni, P. Horcajada, M. Noiray, M. Malanga, A. Aykac, L. Jicsinszky, A. Vargas-Berenguel, N. Semiramoth, S. Daoud-Mahammed, V. Nicolas, C. Martineau, F. Taulelle, J. Vigneron, A. Etcheberry, C. Serre, R. Gref, A "Green" Strategy to Construct Non-Covalent, Stable and Bioactive Coatings on Porous MOF Nanoparticles, *Sci. Rep.,* 2015, **5**, 1-7.
23 C. Orellana-Tavra, S. A. Mercado, D. Fairen-Jimenez, Endocytosis Mechanism of Nano Metal-Organic Frameworks for Drug Delivery, *Adv. Healthcar. Mater.,* 2016, **5**, 2261-2270.
24 L. Guo, Y. Chen, T. Wang, Y. Yuan, Y. Yang, X. Luo, S. Hu, J. Ding, W. Zhou, Rational Design of Metal-Organic Frameworks to Deliver Methotrexate for Targeted Rheumatoid Arthritis Therapy, *J. Control. Release* 2021, **330**, 119-131.

25 Z. Li, Y. Peng, X. Pang, B. Tang, Potential Therapeutic Effects of Mg/HCOOH Metal Organic Framework on Relieving Osteoarthritis, *ChemMedChem,* 2020, **15**, 13-16.
26 Y. Liu, Y. Cheng, H. Zhang, M. Zhou, Y. Yu, S. Lin, B. Jiang, X. Zhao, L. Miao, C. -W. Wei, Q. Liu, Y. -W. Lin, Y. Du, C. J. Butch, H. Wei, Integrated Cascade Nanozyme Catalyzes *In Vivo* ROS Scavenging for Anti-Inflammatory Therapy, *Sci. Adv.,* 2020, **6**, eabb2695.
27 Y. Wang, T. Ying, J. Li, Y. Xu, R. Wang, Q. Ke, S. G. F. Shen, H. Xu, K. Lin, Hierarchical Micro/Nanofibrous Scaffolds Incorporated with Curcumin and Zinc Ion Eutectic Metal Organic Frameworks for Enhanced Diabetic Wound Healing Via Anti-Oxidant and Anti-Inflammatory Activities, *Chem. Eng. J.,* 2020, **402**, 126273.
28 Y. Yin, J. Yang, Y. Pan, Y. Gao, L. Huang, X. Luan, Z. Lin, W. Zhu, Y. Li, Y. Song, Mesopore to Macropore Transformation of Metal-Organic Framework for Drug Delivery in Inflammatory Bowel Disease, *Adv. Healthcar. Mater.,* 2021, **10**, 2000973.
29 F. Zhou, J. Mei, S. Yang, X. Han, H. Li, Z. Yu, H. Qiao, T. Tang, Modified ZIF-8 Nanoparticles Attenuate Osteoarthritis by Reprogramming the Metabolic Pathway of Synovial Macrophages, *ACS Appl. Mater. Interfaces,* 2020, **12**, 2009-2022.
30 X. Lai, S. Wang, M. Hu, Y. Sun, M. Chen, M. Liu, G. Li, Y. Deng, Dual Targeting Single Arrow: Neutrophil-Targeted Sialic Acid-Modified Nanoplatform for Treating Comorbid Tumors and Rheumatoid Arthritis, *Int. J. Pharm.,* 2021, **607**, 121022.
31 S. Wang, X. Lai, C. Li, M. Chen, M. Hu, X. Liu, Y. Song, Y. Deng, Sialic Acid-Conjugate Modified Doxorubicin Nanoplatform for Treating Neutrophil-Related Inflammation, *J. Controlled Release,* 2021, **337**, 612-627.
32 G. D'Arrigo, G. Navarro, C. Di Meo, P. Matricardi, V. Torchilin, Gellan Gum Nanohydrogel Containing Anti-Inflammatory and Anti-Cancer Drugs: A Multi-Drug Delivery System for a Combination Therapy in Cancer Treatment, *Eur. J. Pharm. Biopharm.,* 2014, **87**, 208-216.
33 M. Panchal, F. Nouar, C. Serre, M. Benzaqui, S. Sene, N. Steunou, M. Giménez Marqués, Low Temperature Process for the Synthesis of MOF Carboxylate Nanoparticles. US 20210277042, 2021.
34 S. Dai, A. Tissot, C. Serre, Metal-Organic Frameworks: From Ambient Green Synthesis to Applications, *Bull. Chem. Soc. Jpn.,* 2021, **94**, 2623-2636.
35 M. Benzaqui, M. Wahiduzzaman, H. Zhao, Md R. Hasan, T. Steenhaut, A. Saad, J. Marrot, P. Normand, J.-M. Grenèche, N. Heymans, G. De Weireld, A. Tissot, W. Shepard, Y. Filinchuk, S. Hermans, F. Carn, M. Manlankowska, C. Téllez, J. Coronas, G. Maurin, N. Steunou, C. Serre, A Robust Eco-Compatible Microporous Iron Coordination Polymer for $CO_2$ Capture, *J. Mater. Chem. A,* 2022, **10**, 8535-8545.
36 L. Vayssieres, C. Chaneac, E. Tronc, J. P. Jolivet, Size Tailoring of Magnetite Particles Formed by Aqueous Precipitation: An Example of Thermodynamic Stability of Nanometric Oxide Particles, *J. Colloid Interface Sci.,* 1998, **205**, 205-212.
37 A. Bee, R. Massart, S. Neveu, Synthesis of Very Fine Maghemite Particles, *J. Magn. Magn. Mater.,* 1995, **149**, 6-9.
38 A. García Márquez, A. Demessence, A. E. Platero-Prats, D. Heurtaux, P. Horcajada, C. Serre, J.-S. Chang, G. Férey, V. A. de la Peña-O'Shea, C. Boissière, D. Grosso, C. Sanchez, Green Microwave Synthesis of MIL-100 (Al, Cr, Fe) Nanoparticles for Thin-Film Elaboration, *Eur. J. Inorg. Chem.,* 2012, 5165-5174.
39 I. Christodoulou, T. Bourguignon, X. Li, G. Patriarche, C. Serre, C. Marlière, R. Gref, Degradation Mechanism of Porous Metal-Organic Frameworks by *In Situ* Atomic Force Microscopy, *Nanomaterials,* 2021, **11**, 722.
40 E. Bellido, M. Guillevic, T. Hidalgo, M. J. Santander-Ortega, C. Serre, P. Horcajada, Understanding the Colloidal Stability of the Mesoporous MIL-100(Fe) Nanoparticles in Physiological Media, *Langmuir,* 2014, **30**, 5911-5920.
41 D. Wang, J. Zhou, R. Chen, R. Shi, G. Xia, S. Zhou, Z. Liu, N. Zhang, H. Wang, Z. Guo, Q. Chen, Magnetically Guided Delivery of DHA and Fe Ions for Enhanced Cancer Therapy Based On pH-Responsive Degradation of DHA-Loaded $Fe_3O_4$@C@MIL-100(Fe) Nanoparticles, *Biomaterials,* 2016, **107**, 88-101.
42 J. Volatron, F. Carn, J. Kolosnjaj-Tabi, Y. Javed, Q. L. Vuong, Y. Gossuin, C. Menager, N. Luciani, G. Charron, M. Hémadi, D. Alloyeau, F. Gazeau, Ferritin Protein Regulates the Degradation of Iron Oxide Nanoparticles, *Small,* **2017**, *13*, 1602030.
43 S. Jayashree, K. Nirekshana, G. Guha, D. Bhakta-Guha, Cancer Chemotherapeutics in Rheumatoid Arthritis: A Convoluted Connection, *Biomed. Pharmacother.,* 2018, **102**, 894-911.
44 R. Heo, D. G. You, W. Um, K. Y. Choi, S. Jeon, J. -S. Park, Y. Choi, S. Kwon, K. Kim, I. C. Kwon, D. -G. Jo, Y. M. Kang, J. -H. Park, Dextran Sulfate Nanoparticles as a Theranostic Nanomedicine for Rheumatoid Arthritis, *Biomaterials,* 2017, **131**, 15-26.
45. G. Choi, T.-H. Kim, J.-M. Oh, J.-H. Choy, Emerging Nanomaterials with Advanced Drug Delivery Functions; Focused on Methotrexate Delivery. *Coord. Chem. Rev.,* 2018, **359**, 32-51.
46. M. Cagel, E. Grotz, E. Bernabeu, M. A. Moretton, D. A. Chiappetta, Doxorubicin: Nanotechnological Overviews

from Bench to Bedside. *Drug Discov. Today,* 2017, **22**, 270-281.
47 W. Lin, Y. Cui, Y. Yang, Q. Hu, G. Qian, A Biocompatible Metal-Organic Framework As a pH and Temperature Dual-Responsive Drug Carrier, *Dalton Trans.,* 2018, **47**, 15882-15887.
48 M. D. Rowe, D. H. Thamm, S. L. Kraft, S. G. Boyes, Polymer-Modified Gadolinium Metal-Organic Framework Nanoparticles Used As Multifunctional Nanomedicines for the Targeted Imaging and Treatment of Cancer, *Biomacromolecules,* 2009, **10**, 983-993.
49 W. Lin, Q. Hu, K. Jiang, Y. Cui, Y. Yang, G. Qian, A Porous Zn-Based Metal-Organic Framework for pH and Temperature Dual-Responsive Controlled Drug Release, *Microporous Mesoporous Mater.,* 2017, **249**, 55-60.
50 W. Lin, Q. Hu, K. Jiang, Y. Yang, Y. Yang, Y. Cui, G. Qian, A Porphyrin-Based Metal-Organic Framework As a pH-Responsive Drug Carrier, *J. Solid State Chem.,* 2016, **237**, 307-312.
51 T. Kundu, S. Mitra, P. Patra, A. Goswami, D. Diaz Diaz, R. Banerjee, Mechanical Downsizing of a Gadolinium(III)-Based Metal-Organic Framework for Anticancer Drug Delivery, *Chem. Eur. J.,* 2014, **20**, 10514-10518.
52 I. B. Vasconcelos, T. G. da Silva, G. C. G. Militão, T. A. Soares, N. M. Rodrigues, M. O. Rodrigues, N. B. da Costa Jr., R. O. Freire, S. A. Junior, Cytotoxicity and Slow Release of the Anti-Cancer Drug Doxorubicin from ZIF-8, *RSC Adv.,* 2012, **2**, 9437-9442.
53 X. -G. Wang, Z. -Y. Dong, H. Cheng, S. -S. Wan, W. -H. Chen, M. -Z. Zou, J. -W. Huo, H. -X. Deng, X. -Z. Zhang, A Multifunctional Metal-Organic Framework Based Tumor Targeting Drug Delivery System for Cancer Therapy, *Nanoscale,* 2015, **7**, 16061-16070.
54 X. Zhao, S. Liu, C. Hu, Y. Liu, M. Pang, J. Lin, Controllable Synthesis of Monodispersed NU-1000 Drug Carrier for Chemotherapy, *ACS Appl. Bio Mater.,* 2019, **2**, 4436-4441.
55 X. Wang, B. Yang, X. Xu, M. Su, M. Xi, Z. Yin, Dextran Sulfate-Modified pH-Sensitive Layered Double Hydroxide Nanocomposites for Treatment of Rheumatoid Arthritis, *Drug Deliv. Transl. Res.,* **2021**, *11*, 1096-1106.
56 M. M. Alam, H. S. Han, S. Sung, J. H. Kang, K. H. Sa, H. Al Faruque, J. Hong, E. J. Nam, I. S. Kim, J. H. Park, Y. M. Kang Endogenous Inspired Biomineral-Installed Hyaluronan Nanoparticles as pH-responsive Carrier of Methotrexate for Rheumatoid Arthritis, *J. Controlled Release,* 2017, **252**, 62-72.
57 Y. Wang, J. Yan, N. Wen, H. Xiong, S. Cai, Q. He, Y. Hu, D. Peng, Z. Liu, Y. Liu, Metal-Organic Frameworks for Stimuli-Responsive Drug Delivery, *Biomaterials,* 2020, **230**, 119619.
58 S. Mateen, S. Moin, A. Zafar, A. Q. Khan, Redox Signaling in Rheumatoid Arthritis and the Preventive Role of Polyphenols, *Clin. Chim. Acta,* 2016, **463**, 4-10.
59 S. Mura, J. Nicolas, P. Couvreur, P. Stimuli-Responsive Nanocarriers for Drug Delivery, *Nat. Mater.,* 2013, **12**, 991-1003.
60 Q. Sun, Z. Wang, B. Liu, F. He, S. Gai, P. Yang, D. Yang, C. Li, J. Lin, Recent Advances on Endogenous/Exogenous Stimuli-Triggered Nanoplatforms for Enhanced Chemodynamic Therapy, *Coord. Chem. Rev.,* 2022, **451**, 214267.
61 Y. Zhu, N. Xin, Z. Qiao, S. Chen, L. Zeng, Y. Zhang, D. Wei, J. Sun, H. Fan, Bioactive MOFs Based Theranostic Agent for Highly Effective Combination of Multimodal Imaging and Chemo-Phototherapy, *Adv. Healthcar. Mater.,* 2020, **9**, 2000205.
62 R. Anand, F. Borghi, F. Manoli, I. Manet, V. Agostoni, P. Reschiglian, R. Gref, S. Monti, Host-Guest Interactions in Fe(III)-Trimesate MOF Nanoparticles Loaded with Doxorubicin, *J. Phys. Chem. B,* 2014, **118**, 8532-8539.
63 J. Liu, M. Wu, Y. Pan, Y. Duan, Z. Dong, Y. Chao, Z. Liu, B. Liu, Biodegradable Nanoscale Coordination Polymers for Targeted Tumor Combination Therapy with Oxidative Stress Amplification, *Adv. Funct. Mater.,* 2020, **30**, 1908865.
64 J. K. Gambhir, P. Lali, A. K. Jain, Correlation Between Blood Antioxidant Levels and Lipid Peroxidation in Rheumatoid Arthritis, *Clin. Biochem.,* 1997, **30**, 351-355.
65 M. Yang, J. Ding, X. Feng, F. Chang, Y. Wang, Z. Gao, X. Zhuang, X. Chen, Scavenger Receptor-Mediated Targeted Treatment of Collagen-Induced Arthritis by Dextran Sulfate-Methotrexate Prodrug, *Theranostics,* 2017, **7**, 97-105.
66 M. Yang, J. Ding, Y. Zhang, F. Chang, J. Wang, Z. Gao, X. Zhuang, X. Chen, Activated Macrophage-Targeted Dextran-Methotrexate/Folate Conjugate Prevents Deterioration of Collagen-Induced Arthritis in Mice, *J. Mater. Chem. B,* 2016, **4**, 2102-2113.
67 M. Chen, J. C. K. Amerigos Daddy, Z. Su, N. E. I. Guissi, Y. Xiao, L. Zong, Q. Ping, Folate Receptor-Targeting and Reactive Oxygen Species-Responsive Liposomal Formulation of Methotrexate for Treatment of Rheumatoid Arthritis, *Pharmaceutics,* 2019, **11***,582*.
68 E. Ploetz, A. Zimpel, V. Cauda, D. Bauer, D. C. Lamb, C. Haisch, S. Zahler, A. M. Vollmar, S. Wuttke, H. Engelke, Metal-Organic Framework Nanoparticles Induce Pyroptosis in Cells Controlled by the Extracellular pH, *Adv. Mater.,* 2020, **32**, 1907267.

69 D. Tang, R. Kang, T. V. Berghe, P. Vandenabeele, G. Kroemer, The Molecular Machinery of Regulated Cell Death, *Cell Res.,* 2019, **29**, 347-364.
70 K. Nakamura, T. Fujiwara, T. Ishii, H. Harigae, K. Ogasawara, Cellular Labile Iron Activates NLRP3 Inflammasome, *Blood,* 2014, **124**, 2723-2723.
71 C. Orr, E. Vieira-Sousa, D. L. Boyle, M. H. Buch, C. D. Buckley, J. D. Canete, A. I. Catrina, E. H. S. Choy, P. Emery, U. Fearon, A. Filer, D. Gerlag, F. Humby, J. D. Isaacs, S. A. Just, B. R. Lauwerys, B. Le Goff, A. Manzo, T. McGarry, I. B. McInnes, A. Najm, C. Pitzalis, A. Pratt, M. Smith, P. P. Tak, S. W. Tas, R. Thurlings, J. E. Fonseca, D. J. Veale, Synovial Tissue Research: A State-of-the-art Review, *Nat. Rev. Rheumatol.,* 2017**, 13**, 463-475.
72 B. Guo, D. J. Villeneuve, S. L. Hembruff, A. F. Kirwan, D. E. Blais, M. Bonin, A. M. Parissenti, Cross-Resistance Studies of Isogenic Drug-Resistant Breast Tumor Cell Lines Support Recent Clinical Evidence Suggesting That Sensitivity to Paclitaxel May Be Strongly Compromised by Prior Doxorubicin Exposure, *Breast Cancer Res. Treat.,* 2004**, 85**, 31-51.
73 Q. L. Vuong, J. F. Berret, J. Fresnais, Y. Gossuin, O. Sandre, A Universal Scaling Law to Predict the Efficiency of Magnetic Nanoparticles As MRI $T_2$-Contrast Agents, *Adv. Healthcar. Mater.,* 2012**, 1**, 502-512.
74 M. F. Casula, P. Floris, C. Innocenti, A. Lascialfari, M. Marinone, M. Corti, R. A. Sperling, W. J. Parak, C. Sangregorio, Magnetic Resonance Imaging Contrast Agents Based on Iron Oxide Superparamagnetic Ferrofluids, *Chem. Mater.,* 2010**, 22**, 1739-1748.
75 J. Lin, P. Xin, L. An, Y. Xu, C. Tao, Q. Tian, Z. Zhou, B. Hu, S. Yang, $Fe_3O_4$-ZIF-8 Assemblies As pH and Glutathione Responsive $T_2$-$T_1$ Switching Magnetic Resonance Imaging Contrast Agent for Sensitive Tumor Imaging *In Vivo*, *Chem. Commun.,* 2019**, 55**, 478-481.
76 Z. Xu, Y. Chen, M. Chen, W. Chen, Y. Cheng, Assembly of USPIO/MOF Nanoparticles with High Proton Relaxation Rates for Ultrasensitive Magnetic Resonance Sensing, *J. Mater. Chem. C,* 2021**, 9**, 11915-11923.

Table of Contents

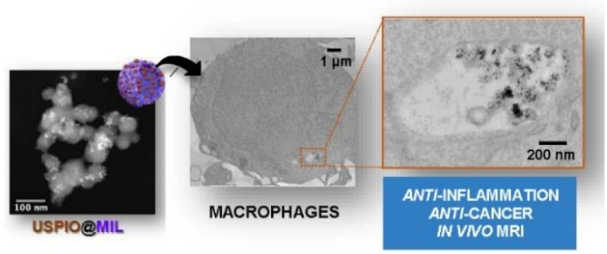


We report a novel superparamagnetic stimuli-responsive nano-object coupling MIL-100(Fe) and maghemite, which, once combined with two complementary drugs (MTX, Dox), leads to a multifunctional theranostic platform to treat inflammatory diseases.